# Atmospheric $CO_2$ estimates for the Miocene to Pleistocene based on foraminiferal $\delta^{11}B$ at Ocean Drilling Program Sites 806 and 807 in the Western Equatorial Pacific

Maxence Guillermic[1,2], Sambuddha Misra[3,4], Robert Eagle[1,2], Aradhna Tripati[1,2]

[1]Department of Atmospheric and Oceanic Sciences, Department of Earth, Planetary, and Space Sciences, Center for Diverse Leadership in Science, Institute of the Environment and Sustainability, University of California – Los Angeles, Los Angeles, CA 90095 USA

[2]Laboratoire Géosciences Océan UMR6538, UBO, Institut Universitaire Européen de la Mer, Rue Dumont d'Urville, 29280, Plouzané, France

[3] Indian Institute of Science, Centre for Earth Sciences, Bengaluru, Karnataka 560012, India

[4] The Godwin Laboratory for Palaeoclimate Research, Department of Earth Sciences, University of Cambridge, UK

*Correspondence to:* Maxence Guillermic (maxence.guillermic@gmail.com) and Aradhna Tripati (atripati@g.ucla.edu)

## ABSTRACT

Constraints on the evolution of atmospheric $CO_2$ levels throughout Earth's history are foundational to our understanding of past variations in climate. Despite considerable effort, records vary in their temporal and spatial coverage and estimates of past $CO_2$ levels do not always converge, and therefore new records and proxies are valuable. Here we reconstruct atmospheric $CO_2$ values across major climate transitions over the past 16 million years using the boron isotopic composition ($\delta^{11}B$) of planktic foraminifera from 89 samples obtained from two sites in the West Pacific Warm Pool, Ocean Drilling Program (ODP) Sites 806 and 807 measured using high-precision multi-collector inductively-coupled plasma mass spectrometry. We compare our results to published data from Pacific Site 872, also in the Western Equatorial Pacific, that goes back to 22 million years ago. These sites are in a region that today is near equilibrium with the atmosphere and are thought to have been in equilibrium with the atmosphere for the interval studied. We show that data from this region is consistent with ice core data and other boron-based studies. The data show evidence for elevated $pCO_2$ during the Middle Miocene and Early to Middle Pliocene, and reductions in $pCO_2$ of ~200 ppm during the Middle Miocene Climate Transition, ~250 ppm during Pliocene Glacial Intensification, and ~50 ppm during the Mid-Pleistocene Climate Transition. There is possible evidence for a larger reduction in glacial $pCO_2$ during the Mid-Pleistocene Transition compared to interglacial $pCO_2$, and a minimum in $pCO_2$ during glacial MIS 30. Our results are consistent with a coupling between $pCO_2$, temperature and ice sheet expansion from the Miocene to Recent.


## Highlights

In this study, we reconstruct atmospheric $pCO_2$ using $\delta^{11}B$ data from ODP Sites 806 and 807 and compare them with ice core data, demonstrating the fidelity of our approach. We therefore apply the same framework to older samples to create a long-term pH and $pCO_2$ reconstruction for the past 16 million years, and recalculate $pCO_2$ for ODP Site 872 from 17 to 22 million years ago. We find major increases in surface water pH and decreases in atmospheric $pCO_2$ were associated with decreased temperature in the Western Equatorial Pacific, including associated with major episodes of ice sheet expansion in the high latitudes, providing more robust quantitative constraints on the past coupling between $pCO_2$, temperature, and cryosphere stability.

**Keywords**

Boron isotopes, $CO_2$, ODP Site 806, ODP Site 807, Miocene, climate

## 1. Introduction

Due to concerns about the long-term consequences of anthropogenic emissions and associated climate change (IPCC, 2014, 2018), efforts have been made to quantify past atmospheric $CO_2$ and examine past relationships between $CO_2$ and temperature. Such data are not only critical for constraining Earth-system sensitivity (Lea, 2004; Lunt et al., 2010; Pagani et al., 2010; Hansen et al., 2012, 2013, Foster and Rohling, 2013; Schmittner et al., 2011; Tierney et al., 2020), but are also of broad interest because such data can help us understand the evolution of climate and geological systems through Earth's history (Tripati et al., 2011; Foster et al., 2017; Tripati and Darby, 2018). However, discrepancies between proxy reconstructions still exist, including for major climate transitions of the Cenozoic. In particular, there remains a pressing need for robust and higher-resolution atmospheric $CO_2$ records from sites that are in equilibrium with the atmosphere.

High-resolution and direct determinations of atmospheric $CO_2$ are available for the last 800 kyr through analysis of air bubbles extracted from ice-cores, but these records are limited to the availability of cores (Petit et al., 1999; Siegenthaler et al., 2005; Lüthi et al., 2008; Bereiter et al., 2015). A window into atmospheric $CO_2$ levels comes from 1 million-year-old blue ice (Higgins et al., 2015) and more recently a snapshot from the early Pleistocene period (Yan et al., 2019). Most reconstructions of $CO_2$ for prior to 800 ka are based on indirect terrestrial and marine proxies. Stomata indices for fossil leaves (Van der Burgh, 1993; Royer , 2001), carbon isotope ratios ($\delta^{13}C$) of paleosols (Retallak et al., 2009), $\delta^{13}C$ of alkenones (Pagani et al., 2005; Zhang et al., 2013), B/Ca ratios of surface-dwelling foraminifera (Yu and Hönisch, 2007; Foster, 2008; Tripati et al., 2009, 2011), and boron isotope ratios ($\delta^{11}B$) of surface-dwelling foraminifera (Pearson and Palmer., 2000; Hönisch et al., 2009; Bartoli et al., 2011; Foster, 2008, 2012; Foster and Sexton, 2014; Chalk et al., 2017; Sosdian et al., 2018; Dyez et al., 2018) have been used to estimate atmospheric $CO_2$.

Each of the above proxy methods has sources of systematic errors that we do not attempt to exhaustively document as they have been discussed in-depth elsewhere (e.g., Pagani et al., 2005; Tripati et al., 2011; Guillermic et al., 2020). However, we note that significant developments in the boron-based proxies include improvements to the accuracy and precision of measurements using multi-collector inductively coupled mass spectrometry (MC-ICP-MS) compared to early work with thermal ionization

mass spectrometry (TIMS), where there were large instrumental mass fractionations and challenges with laboratory intercomparison (Foster et al., 2013; Farmer et al., 2016; Aggarwal and You, 2017). There was also the realization that temperature-dependent $K_D$ to interpreting B/Ca sensitivities observed from the field of sediment trap, core-top, and downcore studies (Yu and Hönisch, 2007; Foster et al., 2008; Tripati et al., 2009, 2011; Babila et al., 2010; Osborne et al., 2020) differ from foraminiferal culture experiments (Allen et al., 2011, 2012) and inorganic calcite (Mavromatis et al., 2015); this type of discrepancy has also been observed with other elemental proxies (e.g., Mg/Ca). Such differences may be due to differences in growth rates (Sadekov et al., 2014), ontogenetic changes, a correlation in the field between temperature and other hydrographic variables that obscure robust statistical determination of parameter relationships, culture conditions resulting in organisms being stressed, and/or other factors.

The marine $CO_2$ proxy that appears to be subject to the fewest systematic uncertainties, based on our current understanding, is the boron isotopic composition ($\delta^{11}B$) of planktic foraminifera as measured using MC-ICPMS and TE-NTIMS (Hain et al., 2018). This proxy provides constraints on seawater pH, if temperature, salinity, seawater $\delta^{11}B$, and the appropriate mono-specific calibration between $\delta^{11}B_{carbonate}$ and $\delta^{11}B_{borate}$ are constrained (Pearson and Palmer, 2000; Foster et al., 2008; Sosdian et al., 2018; Raitzsch et al., 2018; Guillermic et al., 2020). Seawater pH can be used to calculate seawater $pCO_2$ if there are constraints on a second parameter of the carbonate system (e.g. alkalinity, DIC). Atmospheric $pCO_2$ can then be constrained if the site being examined is in air-sea $CO_2$ equilibrium.

Given the evolution of the field, there are relatively few studies generating high-precision boron-based records over major climate transitions in the Cenozoic using recent analytical methods, that incorporate our current understanding of the proxy (e.g., Greenop et al., 2014; Martinez-Boti et al., 2015b; Chalk et al., 2017; Dyez et al., 2018; de la Vega et al., 2020). Furthermore, of the existing studies using boron-based proxies, an additional uncertainty frequently exists, namely the short time interval of study (e.g., emphasizing on a climate transition) (Martinez-Boti et al., 2015b; Chalk et al., 2017) and whether the study sites remain in air-sea $CO_2$ equilibrium with the atmosphere (Martinez et al., 2015a). And although estimation of atmospheric $pCO_2$ from seawater pH using this proxy is relatively straightforward, reconstructions are still impacted by uncertainties including the lack of robust constraints on a second

parameter of the carbonate system, and our limited understanding of secular variations in the $\delta^{11}B$ of seawater (Tripati et al., 2011; Greenop et al., 2017; Sosdian et al., 2018; Rae et al., 2021).

Therefore, to provide additional constraints on the evolution of atmospheric $pCO_2$ from the Miocene through Pleistocene, we developed new records from the western tropical Pacific. We use foraminiferal $\delta^{11}B$ and trace elements in the planktic foraminiferal species *Trilobus sacculifer* and *Globigerinoides ruber* to reconstruct past seawater pH and atmospheric $CO_2$ at Ocean Drilling Program (ODP) Sites 806 and 807 in the Western Equatorial Pacific (WEP) over the last 16 million years (Myr). The sites are located on the western border of the tropical Pacific Ocean, the largest open-oceanic region on the globe, and the warmest open ocean region at present.

These two sites have been examined in other boron-based studies (Wara et al., 2003; Tripati et al., 2009, 2011; Shankle et al., 2020), as has the region more broadly (Pearson and Palmer, 2000), because it is understood to be in equilibrium with the atmosphere and have relative stable hydrography. The region experiences equatorial divergence but is not strongly affected by upwelling and has a current estimated annual air-sea $CO_2$ flux of +28 ppmv (Takahashi et al., 2014). The pre-industrial air-sea $CO_2$ flux is calculated to be +16 ppm, (GLODAP database corrected from anthropogenic inputs), with a value of 298 ppm, compared to the Vostok ice core value of 282 ppm at 1.08 ka . This $pCO_2$ difference is similar to our $pCO_2$ uncertainty (an average of ~17 ppm for the youngest samples). If trade winds were much stronger, and equatorial divergence greater, than this could drive some disequilibrium in the past. However, a few lines of evidence suggest the region was in quasi-equilibrium in the past: 1) zonal temperatures are at a maximum in pre-industrial times and during the Pleistocene, and we are able to reconstruct atmospheric $pCO_2$ values from the ice cores, 2) temperature proxies indicate the region is relatively stable with respect to temperature compared to other parts of the ocean, and also indicate a weak and stable zonal temperature gradient during the Miocene and Pliocene which would support air-sea stable conditions and air-sea equilibrium (e.g., Nathan and Leckie, 2009; Zhang et al. 2014; Liu et al., 2019).

This study builds on low-resolution prior reconstructions for these sites (Wara et al., 2003; Tripati et al., 2009, 2011; Shankle et al., 2020), Site 872 in the tropical Pacific (Sosdian et al., 2018), and other published boron isotope work, to provide additional data to constrain past seawater pH and $pCO_2$ for the

WEP using MC-ICP-MS, thereby providing an invaluable new perspective on reconstructing past atmospheric $CO_2$ via marine sediment archives. We explore various constraints on the second carbonate system parameter using a number of different scenarios, following on the systematic work done by Tripati et al. (2009) and (2011) for B/Ca. We interpret these data using recent constraints on seawater $\delta^{11}B$ (Lemarchand et al., 2000; Raitzsch and Hönisch, 2013; Greenop et al., 2017). For temperature estimation, we utilize a multi-variable model for Mg/Ca (Gray and Evans, 2019), that builds on prior work with clumped isotopes in planktic foraminifera for Site 806 and other WEP sites demonstrating that for the Last Glacial Maximum to recent, salinity-corrected Mg/Ca values are needed to yield convergent estimates of mixed-layer temperatures (Tripati et al., 2014).

## 2. Materials and Methods

Below we describe site locations, analytical methods used, and figures of merit. The supplemental methods section describes screening for potential contamination, equations used for calculations, and error propagation.

### 2.1 Site locations

Samples are from three ODP holes recovered during Leg 130 in the WEP (Fig. 1, Table 1): Hole 806A (0°19.140'N, 159°21.660'E, 2520.7 m water depth), Hole 806B (0°19.110'N, 159°21.660'E, 2519.9 m water depth), and Hole 807A (3°36.420'N, 156°37.500'E, 2803.8 m water depth) (Berger et al., 1993). Sites 806 and 807 are not likely to have experienced major tectonic changes over the last 20 million years.

### 2.2 Preservation

Microfossils in sediments at these sites, as with any sedimentary sequences, have the potential to be influenced by diagenesis. Despite evidence of authigenic carbonate formation, recent modeling work concluded the influence of dissolution and reprecipitation at Sites 806 and 807 was relatively minor (Mitnik et al., 2018). Prior work has also found minimal impacts on the B/Ca ratio of Pliocene foraminifera from Site 806 (White and Ravelo, 2020), and on the Mg/Ca ratio of Miocene *D. altispera* shells at Site 806 (Sosdian et al., 2020). The weight/shell ratio is commonly used to monitor dissolution,

and the only published record at Site 806 for the Pliocene does not show a trend consistent with dissolution of *T. sacculifer* (Wara et al., 2005). We do note that while the "coccolith size-free dissolution" index reported in Si and Rosenthal (2019) indicates higher dissolution rates in the Miocene, their records were thought to be biased from changes in foraminifera assemblages as discussed in White and Ravelo (2020).

To further assess the potential impact of dissolution in our geochemical data, the weight/shell ratio was examined in our samples. The weight/shell data used to monitor dissolution does not exhibit any trend within the interval studied consistent with dissolution. Absolute weights/shell are increasing in the Miocene, which is not consistent with dissolution influencing the record (Fig. 2E). Additionally, reconstructed pH and $pCO_2$ values also exhibit reasonable correspondence with the Vostok ice core data. Downcore $\delta^{11}B$ values from Sites 806 and 807 are similar, despite evidence for higher authigenic carbonate at Site 807 relative to Site 806 (Mitnik et al., 2018). Further, the consistency of our boron isotope and Mg/Ca results with at the two sites with each other, and to the published data from Site 872 (Sosdian et al., 2018), each with different sedimentation rates, are not consistent with diagenesis being a primary driver of the record. Comparison of raw data, and derived parameters, is shown in Figs. 2 and 7.

### 2.3 Age models

The age model for Site 806 from 0-1.35 Ma is based on Medina-Elizalde and Lea (2005); calculated ages correspond well with ages from the Lisiecki and Raymo LR04 stack (Fig. 2A). The fourth polynomial regression-based biostratigraphy from Lear et al. (2015) was used for the rest of the record, following other work (Sosdian et al., 2020). Ages for Site 807 are based on published biostratigraphy (Berger et al., 1993) for 807 with additional constraints placed by Zhang et al., (2007) for the interval from 0-0.55 Ma.

### 2.4 Species and trace element cleaning

Samples were picked and cleaned to remove clays at UCLA (Los Angeles, CA) and the University of Western Brittany (Plouzané, France). 50-100 foraminifera shells were picked from the 300-400μm fraction size for *T. sacculifer* (w/o sacc) and from the 250-300 μm for *G. ruber* (white sensu stricto). Picked foraminifera were gently crushed, clays removed, and checked for coarse-grained silicates.

Samples were then cleaned using a full reductive and oxidative cleaning protocol following Barker et al. (2003). A final leach step with 0.001N HCl was done prior dissolution in 1N HCl. Boron purification used a published microdistillation protocol (see Misra et al., 2014b, Guillermic et al., 2020 for more detailed methods).

### 2.5 Chemical purification and geochemical analysis

Chemical separation was performed in a boron-free clean lab at the University of Cambridge (Cambridge, UK). Calcium concentrations were measured on an ICP-AES ®Ultima 2 HORIBA at the Pôle Spectrometrie Océan (PSO), UMR6538 (Plouzané, France). Elemental ratios (e.g. X/Ca ratios) were analyzed on a Thermo Scientific ®Element XR HR-ICP-MS at the PSO, Ifremer (Plouzané, France). Boron isotopic measurements were carried out on a Thermo Scientific ®Neptune+ MC-ICP-MS equipped with $10^{13}$ Ohm resistor amplifiers (Lloyd et al., 2018) at the University of Cambridge (Cambridge, UK).

### 2.6 Standards

Variations in B isotope ratios are expressed in conventional delta (δ) notation with $\delta^{11}B$ values reported against the reference standard NIST SRM 951 (NIST, Gaithersburg, MD, USA):

$$\delta^{11}B\ (‰) = 1000 \times \left(\frac{^{11}B/^{10}B_{Sample}}{^{11}B/^{10}B_{NIST\ SRM\ 951}} - 1\right) \qquad \textbf{eq. 1}$$

Multiple analyses of external standards were performed to ensure data quality. For boron isotopic measurements, $JC_{P}$-1 (Geological Survey of Japan, Tsukuba, Japan, Gutjahr et al., 2020) was used as a carbonate standard, and NEP, a *Porites sp* coral from University of Western Australia and Australian National University was also used (McCulloch et al., 2014). A boron isotope liquid standard, ERM© AE121 (certified $\delta^{11}B = 19.9 \pm 0.6$ ‰, SD), was used to monitor reproducibility and drift during each session (Vogl and Rosner, 2012; Foster et al., 2013; Misra et al., 2014b). For trace elements, external reproducibility was determined using the consistency standard Cam-Wuellerstorfi (University of Cambridge) (Misra et al., 2014b).

## 2.7 Figures of Merit

### 2.7.1 $\delta^{11}B$ analyses

Samples measured for boron isotopes typically ranged in concentration from 10 ppb B (~5ng B) to 20 ppb B samples (~10ng B). Sensitivity was 10mV/ppb B (eg. 100mV for 10ppb B) in wet plasma at 50µl/min sample aspiration rate. The intensity of $^{11}B$ for a sample at 10 ppb B was typically 104 ± 15 mV (2 SD, typical session) and closely matched the 98 ± 6 mV (2 SD, typical session) of the standard. Procedural boron blanks ranged from 15 pg B to 65 pg B (contributed to less than 1% of the sample signal). The acid blank during analyses was measured at ≤ 1mV on the $^{11}B$ (which also is < 1% of the sample intensity), and no memory effect was seen within and across sessions.

External reproducibility was determined by analyzing the international standard $JC_P$-1 (Gutjahr et al., 2020) and a *Porites sp.* coral (NEP). The boron isotopic composition of $JC_P$-1 was measured at 24.06 ± 0.20‰ (2 SD, n=6) within error of published values of 24.37 ± 0.32‰, 24.11± 0.43‰ and 24.42 ± 0.28‰ from Holcomb et al. (2015), Farmer et al. (2016) and Sutton et al. (2018), respectively. Average values are $\delta^{11}B_{NEP}$ = 25.72 ± 0.79‰ (2 SD, n=31) determined over 13 different analytical sessions, with each number representing a separately processed sample from this study. These results are within error of published values of 26.20 ± 0.88‰ (2 SD, n = 27) and 25.80 ± 0.89‰ (2 SD, n = 6), from Holcomb et al. (2015) and Sutton et al. (2018), respectively. Data are reported in Supplementary Table B.

### 2.7.2 X/Ca analyses

Trace element (TE) analyses were conducted at a Ca concentration of either 10 or 30 ppm. Typical blanks for a 30 ppm Ca session were: $^{7}Li$ < 2%, $^{11}B$ < 7%, $^{25}Mg$ < 0.2% and $^{43}Ca$ < 0.02%. Additionally, blanks for a 10 ppm Ca session were: $^{7}Li$ < 2.5%, $^{11}B$ < 10%, $^{25}Mg$ < 0.4% and $^{43}Ca$ < 0.05%. Analytical uncertainty of a single measurement was calculated from the reproducibility of the CamWuellestorfi standard: 0.6 µmol/mol for Li/Ca, 8 µmol/mol for B/Ca and 0.02 mmol/mol for Mg/Ca (2 SD, n=48). Data are reported in Supplementary Table B.

## 2.8 Calculations

Detailed calculations can be found in the supplemental materials. Briefly, Mg/Ca was used to reconstruct sea surface temperature (SST) using the framework from Gray and Evans. (2019) correcting for influences of pH and salinity. $\delta^{11}B_{carbonate}$ was corrected using an empirical $\delta^{11}B_{carbonate}$-weight/shell ratio relationship. $\delta^{11}B_{borate}$ was determined using species dependent sensitivities of $\delta^{11}B_{carbonate}$ to $\delta^{11}B_{borate}$ (Guillermic et al., 2020). pH was calculated using the $\delta^{11}B_{borate}$ with different scenarios of secular seawater $\delta^{11}B$ changes (Lemarchand et al., 2002; Raitzsch and Hönisch, 2013; Greenop et al., 2017). $pCO_2$ was reconstructed using pH based $\delta^{11}B_{carbonate}$ and different scenarios of Alkalinity (Tyrell and Zeebe, 2004; Ridgwell and Zeebe, 2005; Caves et al. 2016 and Rae et al. 2021). Further details including equations are in the Supplement.

## 3. Results and discussion

### 3.1 Geochemical results

Geochemical data used in this study are presented in Figure 2. Mg/Ca data (Fig. 2C) are consistent with previously published Mg/Ca values for Site 806 on *T. sacculifer* (Wara et al., 2005; Tripati et al., 2009; Nathan and Leckie, 2009). Although the record we generated does not overlap with Site 872, they are time-adjacent, and there is a good correspondence with our Mg/Ca data and the published Mg/Ca record from *T. trilobus* at Site 872 (Sosdian et al., 2018). Mg/Ca from a different species, *D. altispira* (Sosdian et al., 2020), is also plotted with an offset, for comparison.

Comparison with Site 872 data that is part of the compilation from Sosdian et al. (2018) shows that their $\delta^{11}B$ data are in line with our dataset (Figure 2B), and all sites examined in the WEP (Sites 806, 807, and 872) are above the lysocline (Kroenke et al. 1991). The $\delta^{11}B$ data for *T. sacculifer* exhibit a significant decrease (4.2‰) from the Miocene to present. Figure 2B also compares the $\delta^{11}B$ data used in this study with published data from other sites, and shows that raw $\delta^{11}B$ data for the WEP can be lower than values for other regions.

### 3.2 Reproducing $pCO_2$ from ice cores

Validation of air-sea equilibrium in the WEP during the relatively large amplitude late Pleistocene glacial/interglacial cycles was a primary goal for our work. In order to validate our approach, we

reconstructed $pCO_2$ for the last 800 kyr (Fig. 3). The two critical diagnostics we use for method validation are: 1) that the reconstruction of $pCO_2$ is representative of recent atmospheric $CO_2$, and 2) that the boron-based reconstruction empirically reproduces the record from ice cores. For the last 800 kyr, reconstructed $pCO_2$ values for Holes 806A and B and Site 807 are mostly within error of the records from the Vostok and EPICA Dome C ice cores (Fig. 3, Petit et al., 1999, Siegenthaler et al., 2005, Lüthi et al., 2008; compilation from Bereiter et al., 2015), with the exception of two data points at 47 and 79 ka that have lower $pCO_2$ in comparison to ice core values. Crossplots comparing our data are presented in Figs. 3C, 3D, 3E; the slope and intercept are not statistically different from a 1:1 line ($p=0.69$ and $p=0.48$). Between MIS 7 and 6, our reconstructions exhibit a decrease in temperature ($\Delta T$) of 1.2°C, an increase in pH ($\Delta pH$) of 0.08 and a decrease in $pCO_2$ ($\Delta pCO_2$) of 58 ppm. Between stage 3 and 1, we observed an increase of temperature of 2.0°C, a decrease of pH of 0.13 and an increase in $pCO_2$ of 76 ppm. We also compare results with recent reconstructionsin Figs. S1 and S2 (Sosdian et al., 2018; Rae et al., 2021). These results highlight that we are able to reproduce absolute measurements of atmospheric $pCO_2$ of the ice core record, and reproduce the amplitude of changes between transitions, with uncertainties typical for this type of work (Hönisch et al., 2019). We note that reconstructed $pCO_2$ uncertainties could potentially be reduced using independent temperature proxies for the WEP such as clumped isotope thermometry (Tripati et al., 2010; 2014), a technique that is not sensitive to the same sources of error as Mg/Ca thermometry, and therefore is an area planned for future work.

### 3.3 Sea surface temperature in the WEP

Mg/Ca data for the WEP are consistent between studies at Site 806 (Wara et al., 2005; Tripati et al., 2009, 2011; Nathan and Leckie, 2009) and Site 872 (Sosdian et al., 2018). The Mg/Ca in *T. sacculifer* has to date not shown a pH dependency (Gray and Evans, 2019) but Mg/Ca of *G. ruber* does and was therefore corrected from this effect (see supplemental material). Data for both species were corrected from salinity and seawater Mg/Ca changes. Mg/Ca-temperatures for Site 872 was reconstructed using published data and the same framework we use here, and are presented in Figure 4. Recalculated values for Site 872 are from *D. altispera*, with an offset applied relative to *T. sacculifer*, and show similar variations to our record for the MCO-MMCT periods (Sosdian et al., 2020). Temperatures from $Tex_{86}$

and $U^{K'}_{37}$ are plotted for comparison but those records are limited to the last 12 and 5 Myrs respectively (Zhang et al., 2014).

The Mg/Ca data support high temperatures of 35.2 ± 1.3 °C (2SD, n=11) for the early Miocene until the MMCT, with relatively small (ca. 1ºC) change from into the MCO, and larger changes out of the MCO. Similarly warm SST for the MCO were reconstructed in the North Atlantic at Site 608 from $TEX_{86}$ (Super et al., 2018). Despite a gap in our compilation from 11.5 to 9.5 Ma, there is a SST decrease of ~6°C from the MCO to ~7 Ma where temperatures similar to present day values are observed. A decline in temperature during the MMCT is coincident with the timing of a constriction of the Indonesian Seaway, the pre-closure of the trans-equatorial circulation and subsequent formation of a proto-warm pool (Nathan and Leckie, 2009; Sosdian et al., 2020). From 12 to 7 Ma, the Mg/Ca-SST record diverges from $TEX_{86}$ and $U^{K'}_{37}$-based reconstructions, with higher temperatures. At the same time, a record for the North Atlantic showed a decrease of ~10°C from the MCO to ~9 Ma (Super et al., 2018). From 7 Ma to present, the record from multiple proxies – Mg/Ca, $TEX_{86}$, and $U^{K'}_{37}$, in the WEP agree.

### 3.4 Scenarios of seawater $\delta^{11}B$ and alkalinity used for $pCO_2$ reconstructions

Figures 5 and 6 show the different histories of seawater $\delta^{11}B$ and alkalinity used for calculations, respectively. Details of calculations are in the Supplemental methods. Following the approach of Tripati et al. (2009, 2014) and recent literature (Sosdian et al., 2018; Rae et al., 2021), we explored multiple scenarios for the evolution of seawater boron geochemistry (Fig. 5) and alkalinity for calculations of $pCO_2$ (Figs. 6, S1 and S2). During the interval overlapping with the ice core record, we observe that the choice of model used does not make a significant difference in reconstructed values. During earlier time intervals, we see there is a greater divergence, reflecting larger uncertainties in seawater $\delta^{11}B$ and alkalinity further back in Earth history.

Prior to 10 Ma and during the early Pliocene (~4.5 to 3.5 Ma), calculations of $pCO_2$ diverge from published values largely because of the different assumptions each study has used for past seawater $\delta^{11}B$ (Fig. 5). However, we find that when the uncertainty in reconstructed pH is fully propagated, the differences in reconstructed pH values calculated using each of the $\delta^{11}B_{seawater}$ histories is not significantly different (Fig. 5 and 6; see also Hönisch et al., 2019). In contrast to the results from Greenop et al. (2017),

the record from Raitzsch and Hönisch, (2013) exhibits substantial variations on shorter timescales. Such variability is a challenge to reconcile with the Li isotope record of Misra and Froelich, (2012), given that Li has a shorter residence time than boron while having similar sources and sinks. For the remainder of this study, we use the $\delta^{11}B_{seawater}$ history from Greenop et al. (2017) because it is in good agreement with seawater $\delta^{7}Li$ (Misra and Froelich, 2012). The recent calculations of seawater pH (Sosdian et al., 2018; Rae et al., 2021) agree with values from our study when uncertainties are taking into account (Fig. 5).

The four alkalinity models used in this study diverge prior to 9 Ma, with a maximum difference at ~13 Ma that is also reflected in reconstructed $pCO_2$ values (Fig. 6). However, all four models yield $pCO_2$ estimates that are within error of each other when the full uncertainty is considered. Uncertainty in the evolution of seawater alkalinity and seawater $\delta^{11}B$ leads to differences in the absolute values of $pCO_2$ reconstructed (Fig. S2), and a divergence in $pCO_2$ values reconstructed that is largest in the Miocene. The two scenarios that produce the highest divergence in values are those calculated using constant alkalinity relative to those calculated using values from McCaves et al. (2016), with a maximum difference at 15.06 Ma of up to 250 ppm $CO_2$, and with the latter model producing lower values (Fig. 6). Thus, for the MCO, alkalinity is a critical parameter in calculations of absolute $pCO_2$ values. For the Miocene and earlier intervals, improved constraints on past secular variations of seawater $\delta^{11}B$ and alkalinity will yield more accurate reconstructions of $pCO_2$.

For the remainder of this paper, we use the model of Caves et al. (2016) to estimate alkalinity and $\delta^{11}B_{seawater}$ determined by Greenop et al. (2017). We note that two recent syntheses of boron isotope data have been published and compare our results to these findings (Figs. 8 and S2). Sosdian et al. (2018) reports values that are in line with our results in the Miocene but this study does not replicate results from ice cores. Rae et al. (2021) presents reconstructed values that are higher in the Miocene, due to the utilization of different scenarios of seawater $\delta^{11}B$ and alkalinity compared to this work.

### 3.5 Time intervals

#### 3.5.1 Miocene

The study of Miocene climate is thought to provide a useful analog for changes associated with global warming and melting of polar ice, in concert with ocean circulation (Holbourn et al., 2013). The

Miocene epoch (23-5.3 Ma) is characterized by a warm interval, the Miocene Climate Optimum (~17-14.7 Ma - MCO), and an abrupt cooling during the Middle Miocene Climate Transition (~14-13 Ma – MMCT) that led to the expansion of ice on Antarctica and Greenland. Climate modeling supports a role for decreasing $CO_2$ in this transition (DeConto and Pollard, 2003). However, reconstructions for the Miocene are still relatively limited (Sosdian et al., 2018; Rae et al., 2021). Current boron isotope and alkenone-based $pCO_2$ reconstructions support higher $pCO_2$ during the MCO and a decrease over the MMCT (Sosdian et al. 2018; Stoll et al., 2019; Tanner et al., 2020), consistent with what was previously inferred from B/Ca (Tripati et al., 2009, 2011).

We applied the same framework we used for calculations at Sites 806 and 807 to published boron isotope data from Site 872 (Sosdian et al., 2018) in order to extend the WEP record to the early Miocene (Figs. 7, 8). The Miocene data between Sites 806 and 872 do not overlap as both are low in resolution, but do show excellent correspondence in their trends in $\delta^{11}B$ and reconstructed pH. For example, the closest datapoints in time at the two sites are at 15.6 Ma at Site 806 with a $\delta^{11}B$=14.47± 0.21 ‰, and at 16.7 Ma at Site 872, with a $\delta^{11}B$=15.12± 0.25 ‰. The pH values we reconstruct are within error of published estimates from Site 872 (Sosdian et al. 2018, Figs. 7D and 8D). Collectively, these data suggest the early Miocene WEP was characterized by a mixed-layer pH of 8.1 ± 0.1 (2 SD, n=4) between 19.4 and 21.8 Ma, which decreased to reach a minimum during the MCO of 7.7 ($\pm^{0.11}_{0.14}$) ‰.

Given the sensitivity in absolute $pCO_2$ to assumptions about the second carbonate system parameter, a few scenarios were explored for the combined 806/807/872 reconstructed pH values. For all alkalinity scenarios we used, reconstructed $pCO_2$ shows an increase from the Early Miocene to the MCO, with the highest values in the MCO. Recalculated $pCO_2$ for Site 872 between 19.4 and 21.8 Ma is 232 ± 92 ppm (2 SD, n=4), lower but within error of the ones presented in Sosdian et al. (2018) and also within error of a constant alkalinity scenario (Fig 8D). The main difference between reconstructions is when comparing the same data recalculated in Rae et al. (2021) that show higher $pCO_2$ between 19.4 and 21.8 Ma, with an average value of 591 ± 238 ppm (2 SD, n=4) for Site 872, because of the different assumptions used in their study and ours. This difference is important because that would imply a relatively high and stable $pCO_2$ from the early Miocene to MCO, which would imply a decoupling between $pCO_2$ and temperature with no $pCO_2$ change during an interval of decreasing benthic $\delta^{18}O$.

However, our reconstructed $pCO_2$ increase towards the MCO is in line with the observed benthic $\delta^{18}O$ decrease and $\delta^{13}C$ increase and suggest a coupling between temperature and $pCO_2$ over this period. We note that overall, Mg/Ca-SSTs are warm (>32 °C), and there are relatively small changes in Mg/Ca-SST from the early Miocene into the MCO in the WEP.

The highest $pCO_2$ values we reconstruct are during the MCO (Fig. 6E). For the MCO, our estimates are 511 ± 201 ppm (2 SD, n=3, Table 2). The middle Miocene values we reconstruct are in line with previous studies (Greenop et al., 2014; Sosdian et al., 2018). Published $\delta^{11}B$-based reconstructions also support higher $pCO_2$ for the MCO of ~350-400 ppm (Foster et al., 2012) or 300-500 ppm (Greenop et al., 2014) that was recalculated by Sosdian et al. (2018) to be ~470-630 ppm depending on the model of $\delta^{11}B_{seawater}$ chosen. During the MCO relative maxima in $pCO_2$, our data support very warm sea surface temperatures in the WEP (35.6°C ± 0.6°C 2SD, n=3; Fig. 8C), that merits further examination in future studies. In fact, the highest temperatures recorded in our samples occur when there is a minimum in the global composite record of $\delta^{18}O$ of benthic foraminifera (Zachos et al., 2001, 2008; Tripati and Darby, 2018).

During the MMCT, we find evidence for changes in $pCO_2$ and temperature in the WEP (Fig. 8). From 13.5 to 12.7 Ma, we reconstruct an increase of pH ~0.21 and a major decrease of $pCO_2$ of ~215 ppm during an interval highlighted by Flower and Kennett, (1996), who observed changes in $\delta^{18}O$ indicative of rapid East Antarctic Ice Sheet growth, and enhanced organic carbon burial with a maximum $\delta^{13}C$ reached at ~13.6 Ma (Shevenell et al., 2004; Holbourn et al., 2007). As discussed in section 3.4 the alkalinity model used for the calculations have an important impact during the Miocene which is likely responsible for the different absolute $pCO_2$ values over the MCO. In comparison, a scenario of constant alkalinity would lead to a $pCO_2$ during the MCO of 714 ± 313 ppm (2 SD, n=3) and a decrease of ~540 ppm during the MMCT. Both those reconstructions could simulate the large-scale advance and retreat of Antarctic ice with such low $pCO_2$ values (Gasson et al., 2016). At the same time, we find evidence for a decline in SST of 3.4°C to a minimum of 33.3°C. The synchronous shifts in the $\delta^{13}C$ and $\delta^{18}O$ of benthic foraminifera are consistent with increased carbon burial during colder periods, thus feeding back into decreasing atmospheric $CO_2$, and supporting the hypothesis that the drawdown of atmospheric $CO_2$ can in part, be explained by enhanced export of organic carbon.

The resolution of our data during the late Miocene is low, with a data gap from 12.5 to 9.2 Ma, and another gap between 6.5 and 5 Ma. We note the $pCO_2$ peak at ~9 Ma observed by Sosdian et al. (2018) is not seen in our record although this is likely due to the low resolution of our dataset. Between 9.5 and 7.1 Ma we find evidence for a decrease in atmospheric $CO_2$ of 100 ppm associated with a decrease in temperature of 1.3 °C. $pCO_2$ estimates derived from alkenones for Site 1088 (Tanner et al., 2020) do not show the same trend as boron-based reconstructions from the WEP or other regions (Figure 6), but this perhaps is unsurprising given the oceanographic setting of Site 1088.

### 3.5.2 Pliocene

Oxygen isotope data from a global benthic foraminiferal stack show that the Pliocene epoch (5.3-2.6 Ma) was initially characterized by warm conditions followed by the intensification of glaciation that occurred in several steps, including during MIS M2 (3.312-3.264 Ma), followed by the Middle Pliocene Warm Period (Lisiecki and Raymo, 2005). The Middle Pliocene Warm Period (mPWP – 3.29-2.97 Ma) is considered a relevant geological analogue for future climate change given ~3ºC warmer global temperatures and sea levels that were ~20 m higher than today (Dutton et al., 2015; Haywood et al., 2016), and is a target for model intercomparison projects, for which accurate paleo-atmospheric $pCO_2$ estimates are critical (Haywood et al., 2016).

Figure 9 shows that during the Early Pliocene warm interval, from 4.7 to 4.5 Ma, we calculate high $pCO_2$ values of 419 ± 119 ppm (2 SD, n=3, Table 2). The $pCO_2$ data we report provide a higher data density for the Early Pliocene, with a trend that is in line with the reconstruction from Rae et al. (2021). Our data support values of 530 ± 110 ppm over the mPWP (2 SD, n = 4), higher than previously published data (Figs. 9, S2 and Table 2), although we acknowledge our low data density may not fully sample variability over this period. The similarity between our reconstructed values and those published for Site 871 in the Indian Ocean (Sosdian et al., 2018) suggests that changes in Indonesian through-flow do not induce substantial changes in air-sea exchange in the WEP.

The warmth and local $pCO_2$ maxima of the mPWP (mid-Pliocene Warm Period) was followed by a strong decrease of temperature in upwelling and high latitude regions during from 3.3-2.7 Ma, coincident with glacial intensification in the Northern Hemisphere. This climate transition was

hypothesized to be driven by the closure of the Panama seaway the opening of the high latitudes and subsequent modifications of oceanic circulation (Haug and Tiedemann, 1998). However, modeling from Lunt et al. (2008) supports an additional major role for $CO_2$ in the glaciation. $pCO_2$ thresholds have been proposed to explain the intensification of Northern Hemisphere Glaciation, with values proposed ranging from 280 ppm (DeConto et al., 2008) to 200 to 400 ppm (Koening et al., 2011).

The $pCO_2$ concentrations that we calculate indicates a reduction to 350 ppm by 2.7 Ma, ~280 ppm by 2.6 Ma, and ~210 ppm by 2.4 Ma, in several steps. These results support roughly a halving of $CO_2$ values when compared to values of ~530 ppm at 3.3 Ma. These values are consistent with the $pCO_2$ thresholds proposed by both DeConto et al. (2008) and Koening et al. (2011) for the intensification of Northern Hemisphere glaciation and the low atmospheric $CO_2$ (280 ppmv) scenario from Lunt et al. (2008). Mg/Ca SST decline from 30ºC to 26ºC, supporting an Earth System sensitivity of ~4ºC/doubling of $CO_2$ over this range, although given uncertainties, higher values of ~6ºC/doubling of $CO_2$ that have recently been proposed (Tierney et al., 2020) can not be excluded.

We speculate that associated with Pliocene glacial intensification, at 4.42, 3.45 and 2.67 Ma, it is possible that the declines in $CO_2$ and ice growth in turn drove substantial changes in pole-to-equator temperature gradients and winds, that in turn may have impacted iron cycling (Watson et al., 2000; Robinson et al., 2005; Martinez-Garcia et al., 2011), stratification (Toggweiler, 1999; Sigman et al., 2010), and other feedbacks that impact the amplitude of glacial/interglacial cycles and have been implicated as factors that could have contributed to Pliocene glacial intensification. Specifically, as the mean climate state of the planet became cooler, and glacial-interglacial cycles became larger in amplitude, enhanced windiness and dust transport and upwelling during glacials (Martinez-Boti et al., 2015b) may have enhanced iron fertilization and subsequent carbon export (Martinez-Garcia et al., 2011). While data resolution are limited, we speculate this could explain why glacial/interglacial amplitudes in WEP $pCO_2$ values decrease from the MPWP towards the Pleistocene, whereas variations in $\delta^{18}O$ are increasing – a speculation that could be tested with increased data resolution.

### 3.5.3 Pleistocene

During the Pleistocene (2.58-0.01 Ma), the climate system experienced a transition in glacial/interglacial (G/I) variability from low amplitude, higher frequency and obliquity-dominated oscillations (i.e., ~ 41 kyr) of the late Pliocene to the high amplitude, lower frequency and eccentricity-dominated cycles (i.e.., ~100 kyr) of the last 800 kyr. This transition is termed the Middle Pleistocene Transition (1.2-0.8 Ma – MPT). Questions have been raised about the role of atmospheric $CO_2$ during this transition, including using boron-based proxies (Hönisch et al., 2009; Tripati et al., 2011; Chalk et al., 2017). Previous boron isotope studies for ODP Sites 668 and 999 in the tropical Atlantic Ocean have suggested that a decline in atmospheric $CO_2$ did occur during glacial periods in the MPT, but not during interglacials (Hönisch et al., 2009; Chalk et al., 2017; Dyez et al., 2018).

Our $pCO_2$ concentrations for Sites 806/807 reported here are in good agreement with those determined from ice cores from the early Pleistocene (Yan et al., 2019, Figs. 9 and 10), and with the boron-derived $pCO_2$ from a recent compilation (Rae et al., 2021). Results for the MPT are broadly in the range of values reported by Hönisch et al. (2009) and Chalk et al. (2017). Although our data are relatively limited, we note they have greater resolution for the middle and later part of the transition than prior publications that have drawn conclusions about the MPT (Hönisch et al., 2009; Chalk et al., 2017; Dyez et al., 2018) (Fig. 10D) and therefore we explore their implications.

Taken alone, or when combined with the published data from Chalk et al. (2017) (that is also based on MC-ICPMS), our results support a possible reduction of both glacial and interglacial $pCO_2$ values. We also find evidence that during the MPT, glacial $pCO_2$ declined rapidly from 189 (±30) ppm at MIS 36 (Chalk et al., 2017) to reach a minimum of 170 ($\pm^{52}_{24}$) ppm during MIS 30. We note that $pCO_2$ concentrations are within error when uncertainty is fully propagated, and then remained relatively stable until the end of the MPT whereas interglacial $pCO_2$ values decrease gradually to reach post-MPT values.

In our record for the last 16 Myr, the lowest $pCO_2$ is recorded at MIS 30 during the MPT, with values of 164 ($\pm^{44}_{35}$) ppm, which supports an atmospheric $CO_2$ threshold that leads to ice sheet stability. During this transition, the $pCO_2$ threshold needed to build sufficiently large ice sheets that were able to survive the critical orbital phase of rising obliquity to ultimately switch to a 100 kyr world, was likely reached at MIS 30. The multiple feedbacks resulting from stable ice sheets (iron

fertilization/productivity/changes in albedo/ changes in deep water formation) might have sustained larger mean global ice volumes over the subsequent 800 kyr. An asymmetrical decrease between $pCO_2$ values during interglacials relative to glacials, with glacials exhibiting the largest change across the MPT, would have led to increased sequestration of carbon during glacials in the 100 kyr world, as discussed by Chalk et al. (2017), with increased glacial dust input and iron fertilization.

### 3.6 Changes in volcanic activity and silicate weathering, and long-term $pCO_2$

On million-year timescales, atmospheric $CO_2$ is mainly controlled by volcanic activity and silicate weathering. Over the last 16 Myr, two relative maxima in atmospheric $pCO_2$ are observed in our record, one during the MCO (at 15.67 Ma) and a second around the late Miocene/early Pliocene (beginning at 4.7 and 4.5 Ma) (Fig. 11), though the timing for the latter is not precise. The strong $pCO_2$ increase from the early Miocene to MCO is timely with increasing volcanic activity (Foster al. 2012), associated with the eruption of the Columbia River Flood Basalts (Hooper et al., 2002; Kasbohm and Schoene, 2018), with recent geochronologic evidence published supporting higher eruption activity between 16.7 and 15.9 Ma (Kasbohm and Schoene, 2018) reinforcing the idea of an episodic $pCO_2$ increase during the MCO due to volcanic activity.

The second $CO_2$ peak could correspond to observed global increased volcanism in the early/middle Pliocene (Kennett and Thunell, 1977; Kroenke et al., 1993), and/or a change of silicate weathering regime. Strontium and lithium isotopes ($^{87/86}Sr$ and $\delta^7Li$) have been used as proxy for silicate weathering activity. Although the strontium isotope record exhibits a monotonous increase, lithium isotope data (Misra and Froelich, 2012) are more variable with a transition from a period of increase seawater $\delta^7Li$ (e.g. non-steady state weathering) to stable seawater $\delta^7Li$ (e.g., steady state weathering) beginning at roughly 6.8 Ma (Fig. 11).

It is also interesting to note that the changes in $\delta^7Li$ (Fig. 11B) in the early Miocene to the MCO are in line with changes in $pCO_2$. Before 18.5 Ma, the $pCO_2$ is relatively stable, $\delta^7Li$ is increasing representative of a non-steady state weathering. From 18.6 to 16.7 the $\delta^7Li$ decrease of about 2‰, this decrease can inform on decreasing weathering rate and this decrease is associated with an increase in $pCO_2$. Between 16.7 and 15.9 Ma, when the eruption of the Columbia River Flood Basalts is maximum

520 the $\delta^7$Li increases, in line with higher weathering due to higher atmospheric $CO_2$ and the presence of fresh
521 silicate rocks. The $\delta^7$Li decreases again until the end of the MCO ~14.7 Ma, in line with a decrease in the
522 eruption rate and sustaining high atmospheric $CO_2$ , then, a constant increase is observed until the early
523 Pliocene where the change toward a steady in weathering regime occurs, this increase in $\delta^7$Li is also
524 consistent with the decrease in $pCO_2$ observed until the early Pliocene.
525
526 **3.9 Outlook and Conclusions**
527 We developed a reconstruction of atmospheric $pCO_2$ based on $\delta^{11}$B of planktic foraminifera from
528 ODP Sites 806 and 807 located in the Western Equatorial Pacific for the past 16 million years and
529 extended the record to 22 Ma by processing data from Site 872. Our study represents the first long-term
530 reconstruction for the Neogene derived from boron isotopes from the Pacific Ocean. We build on past
531 efforts to reconstruct atmospheric $pCO_2$ using different proxies from this region, including from carbon
532 isotopes in marine organic matter (Rayno et al., 1996) and alkenones (Pagani et al., 2010), as well as
533 foraminiferal B/Ca ratios (Tripati et al., 2009, 2011), all of which have been shown to have a number of
534 complexities and potential sources of systematic error (e.g., Tripati et al., 2011). It also builds on efforts
535 using boron isotopes in other regions using MC-ICP-MS (Seki et al., 2010; Foster et al., 2012, 2014;
536 Greenop et al., 2014; Martinez-Boti et al., 2015b; Stap et al., 2016; Chalk et al., 2017; Dyez et al., 2018;
537 de la Vega et al., 2020), and our recent work constraining fractionation factors and measuring small
538 samples of foraminifera. Although the record is not continuous, with variable resolution, it captures both
539 long-term and short-term variability associated with several key transitions and demonstrates the utility
540 of these sites for future higher resolution study.
541 As expected, these data generally reproduce the $pCO_2$ record from ice cores, consistent with the
542 sites being in equilibrium with the atmosphere. The MCO has higher $pCO_2$ than reconstructions from
543 other sites, with values estimated as 511 ± 201 ppm (2 SD, n=3), likely linked to the eruption of the
544 Columbia River Flood Basalts, with values declining into the early Pliocene, including during Pliocene
545 glacial intensification. The changes in $pCO_2$ we observed are in line with changes in $\delta^7$Li, proxy of silicate
546 weathering, future modellisation on those records will provide helpful insights.

We find support for a larger reduction in glacial $pCO_2$ during the MPT compared to interglacial $pCO_2$, and a minimum in $pCO_2$ during glacial MIS 30. These findings confirm a role for $CO_2$ in the transition from a 41 kyr to a 100 kyr world.

Higher-resolution boron isotope records from the WEP would allow for further resolution of these changes. Additional constraints on temperature, such as from clumped isotopes (Tripati et al., 2010) in the WEP (Tripati et al., 2014), could allow for uncertainties in $pCO_2$ estimates from boron isotopes to be reduced and for new constraints on Earth system climate sensitivity. Future constraints on the vertical structure of the tropical Pacific during these transitions may also potentially be illuminating.

**Code/ data availabilility**

All data are available in the supplemental materials.

**Author Contribution**

AT wrote the proposals that funded the work and provided the samples. All authors contributed to the experimental design. MG performed the measurements with assistance from SM. MG conducted the data analysis. MG drafted the paper, which was edited by all authors. Interpretation was led by MG, AT, and SM with input from RE.

**Competing interests**

The authors declare that they have no conflict of interest.

**Acknowledgments**

The authors wish to thank the Tripati Lab, including Lea Bonnin and Alexandra Villa, for assistance with picking samples; the IODP core repository for provision of samples; Mervyn Greaves for technical support and use of laboratory space at the University of Cambridge; Yoan Germain, Emmanuel Ponzevera, Céline Liorzou and Oanez Lebeau for technical support and use of laboratory space at IUEM and Ifremer (Plouzané, France). We thank Thomas Chalk, another anonymous reviewer, and Hubertus Fischer for their helpful comments on the manuscript, and Mathis Hain for discussion of this work.

**Financial support**

This research is supported by DOE BES grant no. DE-FG02-13ER16402 to AKT, by the International Research Chair Program that is funded by the French government (LabexMer ANR-10-LABX-19-01) to AKT and RAE, and IAGC student research grant 2017.

## 6. References

582 Aggarwal, S. K., & You, C. F.: A review on the determination of isotope ratios of boron with
583 mass spectrometry. Mass Spectrometry Reviews, 36(4), 499-519, 2017.
584 Allen, K. A. and Hönisch, B.: The planktic foraminiferal B/Ca proxy for seawater carbonate
585 chemistry, A critical evaluation, Earth Planet. Sci. Lett, 345–348, 203–211, 2012.
586 Allen, K. A., Hönisch, B., Eggins, S. M., Yu, J., Spero, H. J., Elderfield, H.: Controls on
587 boron incorporation in cultured tests of the planktic foraminifer Orbulina universa. Earth
588 and Planetary Science Letters, 309(3-4), 291-301, 2011.
589 Anagnostou, E., John, E. H., Edgar, K. M., Foster, G. L., Ridgwell, A., Inglis, G. N., D.
590 Pancost, R., J. Lunt, D., Pearson, P. N.: Changing atmospheric CO2 concentration was
591 the primary driver of early Cenozoic climate. Nature, 533(7603), 380-384, 2016.
592 Babila, T., Huang, K. F., Rosenthal, Y., Conte, M. H., & Lin, H. L. Development of B/Ca as
593 a seawater pH proxy using sediment trap time series, abstract, 2010.
594 Badger M. P. S., Chalk T. B., Foster G. L., Bown P. R., Gibbs S. J., Sexton P. F., Schmidt D.
595 N., Pälike H., Mackensen A. and Pancost R. D.: Insensitivity of alkenone carbon
596 isotopes to atmospheric CO2 at low to moderate CO2 levels. Climate of the Past, 15(2),
597 539-554, 2019.
598 Badger M. P. S., Lear C. H., Pancost R. D., Foster G. L., Bailey T. R., Leng M. J. and Abels
599 H. A.: CO2 drawdown following the middle Miocene expansion of the Antarctic Ice
600 Sheet. Paleoceanography 28, 42–53, 2013.
601 Barker S., Greaves M. and Elderfield H.: A study of cleaning procedures used for
602 foraminiferal Mg/Ca paleothermometry. Geochemistry, Geophys. Geosystems 4, 1–20,
603 2003.
604 Bartoli G., Hönisch B. and Zeebe R. E.: Atmospheric CO2 decline during the Pliocene
605 intensification of Northern Hemisphere glaciations. Paleoceanography 26, 1–14, 2011.
606 Berger, W.H., Kroenke, J.W., Mayer, L.A.: Proceedings of the Ocean Drilling Program,
607 Scientific Results, Vol. 130, 1993.
608 Berger, W.H., Kroenke, L., Janecek, T.R., et al., . Proceedings of the Ocean Drilling
609 Program. Initial Reports, p. 130, 1991.
610 Bian, N., & Martin, P. A.: Investigating the fidelity of Mg/Ca and other elemental data from
611 reductively cleaned planktonic foraminifera. Paleoceanography, 25(2), 2010.
612 Bolton C. T. and Stoll H. M.: Late Miocene threshold response of marine algae to carbon
613 dioxide limitation. Nature 500, 558–562, 2013.
614 Bolton C. T., Hernández-Sánchez M. T., Fuertes M.-Á., González-Lemos S., Abrevaya L.,
615 Mendez-Vicente A., Flores J.-A., Probert I., Giosan L., Johnson J. and Stoll H. M. :
616 Decrease in coccolithophore calcification and CO2 since the middle Miocene. Nat.
617 Commun. 7, 10284, 2016.
618 Boyer, T.P., J. I. Antonov, O. K. Baranova, C. Coleman, H. E. Garcia, A. Grodsky, D. R.
619 Johnson, R. A. Locarnini, A. V. Mishonov, T.D. O'Brien, C.R. Paver, J.R. Reagan, D.
620 Seidov, I. V. Smolyar, and M. M. Zweng, 2013: World Ocean Database 2013, NOAA
621 Atlas NESDIS 72, S. Levitus, Ed., A. Mishonov, Technical Ed.; Silver Spring, MD, 209
622 pp., http://doi.org/10.7289/V5NZ85MT, 2013.
623 Brennan, S. T., Lowenstein, T. K., & Cendón, D. I. : The major-ion composition of Cenozoic
624 seawater: The past 36 million years from fluid inclusions in marine halite. American
625 Journal of Science, 313(8), 713-775, 2013.
626 Caves J. K., Jost A. B., Lau K. V. and Maher K.: Cenozoic carbon cycle imbalances and a
627 variable weathering feedback. Earth Planet. Sci. Lett. 450, 152–163, 2016.
628 Chalk T. B., Hain M. P., Foster G. L., Rohling E. J., Sexton P. F., Badger M. P. S., Cherry S.
629 G., Hasenfratz A. P., Haug G. H., Jaccard S. L., Martínez-García A., Pälike H., Pancost

R. D. and Wilson P. A.: Causes of ice age intensification across the Mid-Pleistocene Transition. Proc. Natl. Acad. Sci., 201702143, 2017.
Coggon R. M., Teagle D. A. H. and Dunkley Jones T. Comment on "What do we know about the evolution of Mg to Ca ratios in seawater?" by Wally Broecker and Jimin Yu. Paleoceanography 26, 2011.
DeConto, R. M., & Pollard, D.: Rapid Cenozoic glaciation of Antarctica induced by declining atmospheric CO2. Nature, 421(6920), 245-249, 2003.
DeConto R. M., Pollard D., Wilson P. A., Pälike H., Lear C. H. and Pagani M.: Thresholds for Cenozoic bipolar glaciation. Nature 455, 652–656, 2008.
DeFantle M. S. and DePaolo D. J.: Sr isotopes and pore fluid chemistry in carbonate sediment of the Ontong Java Plateau: Calcite recrystallization rates and evidence for a rapid rise in seawater Mg over the last 10 million years. Geochim. Cosmochim. Acta 70, 3883–3904, 2006.
Dekens P. S., Lea D. W., Pak D. K. and Spero H. J.: Core top calibration of Mg/Ca in tropical foraminifera: Refining paleotemperature estimation. Geochemistry, Geophys. Geosystems 3, 1–29, 2002.
Delaney, M. L., Bé, A. W., & Boyle, E. A.: Li, Sr, Mg, and Na in foraminiferal calcite shells from laboratory culture, sediment traps, and sediment cores. Geochimica et Cosmochimica Acta, 49(6), 1327-1341, 1985.
de la Vega, E., Chalk, T. B., Wilson, P. A., Bysani, R. P., & Foster, G. L.: Atmospheric CO2 during the Mid-Piacenzian Warm Period and the M2 glaciation. Scientific Reports, 10(1), 1-8, 2020.
Dickson A. G.: Thermodynamics of the Dissociation of Boric Acid in Potassium Chloride Solutions from 273.15 to 318.15 K. J. Chem. Eng. Data 35, 253–257, 1990.
Drury, A. J., Lee, G. P., Gray, W. R., Lyle, M., Westerhold, T., Shevenell, A. E., & John, C. M.: Deciphering the state of the late Miocene to early Pliocene equatorial Pacific. Paleoceanography and paleoclimatology, 33(3), 246-263, 2018.
Dyez, K. A., Hönisch, B., & Schmidt, G. A.: Early Pleistocene obliquity-scale pCO2 variability at~ 1.5 million years ago. *Paleoceanography and Paleoclimatology*, *33*(11), 1270-1291, 2018.
Evans, D. & Müller, W.: Deep time foraminifera Mg/Ca paleothermometry: Nonlinear correction for secular change in seawater Mg/Ca. Paleoceanography 27, PA4205, 2012.
Evans, D., Wade, B. S., Henenhan, M., Erez, J., & Müller, W.: Revisiting carbonate chemistry controls on planktic foraminifera Mg/Ca: implications for sea surface temperature and hydrology shifts over the Paleocene–Eocene Thermal Maximum and Eocene–Oligocene transition. Climate of the Past, 12(4), 819-835, 2016.
Farmer, J. R., Hönisch, B., & Uchikawa, J.: Single laboratory comparison of MC-ICP-MS and N-TIMS boron isotope analyses in marine carbonates. Chemical Geology, 447, 173-182, 2016.
Farrell, J.W., Raffi, I., Janecek, T.,Murray, D.W., Levitan,M., Dadey, K.A., Emeis, K.C., Lyle, M., Flores, J.A., Hovan, S: Late Neogene sedimentation patterns in the eastern Equatorial Pacific Ocean. In: Pisias,N.G.,Mayer, L.A., Janecek, T.R., Palmer-Julson, A., van Andel, T.H. (Eds.), Proceedings of the Ocean Drilling Program. Scientific Results, vol. 138. ocean Drilling Program, College Station, TX, pp. 717–756, 1995.
Flower, B. P., & Kennett, J. P.: Middle Miocene deepwater paleoceanography in the southwest Pacific: relations with East Antarctic Ice Sheet development. Oceanographic Literature Review, 8(43), 796, 1996.

677 Ford, H. L., Ravelo, A. C., Dekens, P. S., LaRiviere, J. P., & Wara, M. W.: The evolution of
678 the equatorial thermocline and the early Pliocene El Padre mean state. Geophysical
679 Research Letters, 42(12), 4878-4887, 2015.
680 Foster G. L.: Seawater pH, pCO2and [CO2-3] variations in the Caribbean Sea over the last
681 130 kyr: A boron isotope and B/Ca study of planktic foraminifera. Earth Planet. Sci.
682 Lett. 271, 254–266, 2008.
683 Foster G. L. and Rohling E. J.: Relationship between sea level and climate forcing by CO2 on
684 geological timescales. Proc. Natl. Acad. Sci. 110, 1209–1214, 2013.
685 Foster G. L. and Sexton P. F.: Enhanced carbon dioxide outgassing from the eastern
686 equatorial Atlantic during the last glacial. Geology 42, 1003–1006, 2014.
687 Foster, G. L., Hönisch, B., Paris, G., Dwyer, G. S., Rae, J. W., Elliott, T., Gaillardet, J.,
688 Hemming, N. G., Louvat, P., Vengosh, A.: Interlaboratory comparison of boron isotope
689 analyses of boric acid, seawater and marine CaCO3 by MC-ICPMS and NTIMS.
690 Chemical Geology, 358, 1-14, 2013.
691 Foster G. L., Lear C. H. and Rae J. W. B.: The evolution of pCO2, ice volume and climate
692 during the middle Miocene. Earth Planet. Sci. Lett. 341–344, 243–254, 2012.
693 Foster G. L., Royer D. L. and Lunt D. J.: Future climate forcing potentially without precedent
694 in the last 420 million years. Nat. Commun. 8, 14845.
695 http://dx.doi.org/10.1038/ncomms14845, 2017.
696 Gasson E., DeConto R. M., Pollard D. and Levy R. H.: Dynamic Antarctic ice sheet during
697 the early to mid-Miocene. Proc. Natl. Acad. Sci. 113, 3459–3464, 2016.
698 Gothmann A. M., Stolarski J., Adkins J. F., Schoene B., Dennis K. J., Schrag D. P., Mazur
699 M. and Bender M. L.: Fossil corals as an archive of secular variations in seawater
700 chemistry since the Mesozoic. Geochim. Cosmochim. Acta 160, 188–208, 2015.
701 GraphPad Prism version 7.00 for Windows, GraphPad Software, La Jolla California USA,
702 www.graphpad.com"
703 Gray, W. R., & Evans, D.: Nonthermal influences on Mg/Ca in planktonic foraminifera: a
704 review of culture studies and application to the Last Glacial Maximum.
705 Paleoceanography and Paleoclimatology, 34(3), 306-315, 2019.
706 Gray, W. R., Weldeab, S., Lea, D. W., Rosenthal, Y., Gruber, N., Donner, B., & Fischer, G.:
707 The effects of temperature, salinity, and the carbonate system on Mg/Ca in
708 Globigerinoides ruber (white): A global sediment trap calibration. Earth and Planetary
709 Science Letters, 482, 607-620, 2018.
710 Greenop R., Foster G. L., Wilson P. A. and Lear C. H.: Middle Miocene climate instability
711 associated with high-amplitude CO2 variability. Paleoceanography 29, 845–853, 2014.
712 Greenop R., Hain M. P., Sosdian S. M., Oliver K. I. C., Goodwin P., Chalk T. B., Lear C. H.,
713 Wilson P. A. and Foster G. L.: A record of Neogene seawater δ11B reconstructed from
714 paired δ11B analyses on benthic and planktic foraminifera. Clim. Past 13, 149–170,
715 2017.
716 Guillermic, M., Misra, S., Eagle, R., Villa, A., Chang, F., Tripati, A.,: Seawater pH
717 reconstruction using boron isotopes in multiple planktonic foraminifera species with
718 different depth habitats and their potential to constrain pH and pCO2 gradients.
719 Biogeosciences, 17(13), 3487-3510, 2020.
720 Gutjahr, M., Bordier, L., Douville, E., Farmer, J., Foster, G. L., Hathorne, E. C., J., Foster, G.
721 L., Hathorne, E., Hönish, B., Lemarchand, D., Louvat, P., McCulloch, M., Noireaux, J.,
722 Pallavicini, N., Rodushkin, I., Roux, P., Stewart, J., Thil, F. You, C.F.Sub-permil
723 interlaboratory consistency for solution-based boron isotope analyses on marine
724 carbonates. *Geostandards and Geoanalytical Research*, 2020.

Hain, M. P., Foster, G. L., & Chalk, T.: Robust constraints on past CO2 climate forcing from the boron isotope proxy. Paleoceanography and Paleoclimatology, 33(10), 1099-1115, 2018.
Hansen, J., Sato, M., & Ruedy, R.: Perception of climate change. Proceedings of the National Academy of Sciences, 109(37), 2012.
Hansen J., Sato M., Russell G. and Kharecha P.: Climate sensitivity, sea level and atmospheric carbon dioxide. Philos. Trans. R. Soc. A Math. Phys. Eng. Sci. 371, 1–38, 2013.
Haug, G. H., & Tiedemann, R.: Effect of the formation of the Isthmus of Panama on Atlantic Ocean thermohaline circulation. Nature, 393(6686), 673-676, 1998.
Haywood, A. M., Dowsett, H. J., & Dolan, A. M.: Integrating geological archives and climate models for the mid-Pliocene warm period. Nature communications, 7(1), 1-14, 2016.
Hemming N. G. and Hanson G. N.: Boron isotopic composition and concentration in modern marine carbonates. Geochim. Cosmochim. Acta 56, 537–543, 1992.
Henehan M. J., Foster G. L., Bostock H. C., Greenop R., Marshall B. J. and Wilson P. A.: A new boron isotope-pH calibration for Orbulina universa, with implications for understanding and accounting for 'vital effects.' Earth Planet. Sci. Lett. 454, 282–292, 2016.
Henehan M. J., Rae J. W. B., Foster G. L., Erez J., Prentice K. C., Kucera M., Bostock H. C., Martínez-Botí M. A., Milton J. A., Wilson P. A., Marshall B. J. and Elliott T. (2013) Calibration of the boron isotope proxy in the planktonic foraminifera Globigerinoides ruber for use in palaeo-CO2reconstruction. Earth Planet. Sci. Lett. 364, 111–122, 2013.
Higgins J. A., Kurbatov A. V, Spaulding N. E., Brook E., Introne D. S., Chimiak L. M., Yan Y., Mayewski P. A. and Bender M. L.: Atmospheric composition 1 million years ago from blue ice in the Allan Hills, Antarctica. Proc. Natl. Acad. Sci. 112, 6887–6891, 2015.
Holbourn A., Kuhnt W., Frank M. and Haley B. A.: Changes in Pacific Ocean circulation following the Miocene onset of permanent Antarctic ice cover. Earth Planet. Sci. Lett. 365, 38–50, 2013.
Holcomb M., DeCarlo T. M., Schoepf V., Dissard D., Tanaka K. and McCulloch M.: Cleaning and pre-treatment procedures for biogenic and synthetic calcium carbonate powders for determination of elemental and boron isotopic compositions. Chem. Geol. 398, 11–21, 2015.
Hönisch, B. and Hemming, N. G., Ground-truthing the boron isotope-paleo-pH proxy in planktonic foraminifera shells: Partial dissolution and shell size effects, Paleoceanography 19, 1–13, 2004.
Honisch, B., Allen, K. A., Lea, D. W., Spero, H. J., Eggins, S. M., Arbuszewski, J., deMenocal, P., Rosenthal, Y., D. Russel, a.: Elderfield, H.: The influence of salinity on Mg/Ca in planktic foraminifers–Evidence from cultures, core-top sediments and complementary d 18 O. Geochimica Et Cosmochimica Acta, 121, 196-213, 2013.
Hönisch, B., Eggins, S. M., Haynes, L. L., Allen, K. A., Holland, K. D., & Lorbacher, K.: Boron Proxies in Paleoceanography and Paleoclimatology. John Wiley & Sons, 2019.
Hönisch B., Hemming N. G., Archer D., Siddall M. and McManus J. F.: Atmospheric carbon dioxide concentration across the mid-pleistocene transition. Science 324, 1551–1554, 2009.
Horita J., Zimmermann H. and Holland H. D.: Chemical evolution of seawater during the Phanerozoic: Implications from the record of marine evaporites. Geochim. Cosmochim. Acta 66, 3733–3756., 2002.

IPCC: Climate Change 2014 - The Physical Science Basis, edited by Intergovernmental Panel on Climate Change, Cambridge University Press, Cambridge., 2014.
IPCC: Global Warming of 1.5 ºC- edited by Intergovernmental Panel on Climate Change, 2018.
Johnstone, H. J., Lee, W., & Schulz, M.: Effect of preservation state of planktonic foraminifera tests on the decrease in Mg/Ca due to reductive cleaning and on sample loss during cleaning. Chemical Geology, 420, 23-36, 2016.
Kasbohm, J., & Schoene, B.: Rapid eruption of the Columbia River flood basalt and correlation with the mid-Miocene climate optimum. Science advances, 4(9), eaat8223, 2018.
Kennett, J. P., & Thunell, R. C.: On explosive Cenozoic volcanism and climatic implications. Science, 196(4295), 1231-1234, 1977.
Kısakürek, B., Eisenhauer, A., Böhm, F., Garbe-Schönberg, D., & Erez, J.: Controls on shell Mg/Ca and Sr/Ca in cultured planktonic foraminiferan, Globigerinoides ruber (white). Earth and Planetary Science Letters, 273(3-4), 260-269, 2008.
Klochko K., Kaufman A. J., Yao W., Byrne R. H. and Tossell J. A.: Experimental measurement of boron isotope fractionation in seawater. Earth Planet. Sci. Lett. 248, 261–270, 2006.
Koenig S. J., DeConto R. M. and Pollard D.: Late Pliocene to Pleistocene sensitivity of the Greenland Ice Sheet in response to external forcing and internal feedbacks. Clim. Dyn. 37, 1247–1268, 2011.
Kroenke, L. W., Berger, W. H., Janecek, T. R. and Shipboard Scientific Party: Proceedings of the Ocean Drilling Program, Initial Reports, Vol. 130, 1991.
Lea, D. W.: The 100 000-yr cycle in tropical SST, greenhouse forcing, and climate sensitivity. Journal of Climate, 17(11), 2170-2179, 2004.
Lee, K., Kim, T. W., Byrne, R. H., Millero, F. J., Feely, R. A., & Liu, Y. M.: The universal ratio of boron to chlorinity for the North Pacific and North Atlantic oceans. Geochimica et Cosmochimica Acta, 74(6), 1801-1811, 2010.
Lea, D. W., Pak, D. K., & Spero, H. J.: Climate impact of late Quaternary equatorial Pacific sea surface temperature variations. Science, 289(5485), 1719-1724, 2000.
Lemarchand D., Gaillardet J., Lewin and Allégre C. J.: The influence of rivers on marine boron isotopes and implications for reconstructing past ocean pH. Nature 408, 951–954, 2000.
Lisiecki L. E. and Raymo M. E.: A Pliocene-Pleistocene stack of 57 globally distributed benthic δ18O records. Paleoceanography 20, 1–17, 2005.
Lloyd, N. S., Sadekov, A. Y. and Misra, S., Application of 1013ohm Faraday cup current amplifiers for boron isotopic analyses by solution mode and laser ablation multicollector inductively coupled plasma mass spectrometry, Rapid Commun. Mass Spectrom., 32, 9–18, 2018.
Lueker, T. J., Dickson, A. G., & Keeling, C. D.: Ocean pCO2 calculated from dissolved inorganic carbon, alkalinity, and equations for K1 and K2: validation based on laboratory measurements of CO2 in gas and seawater at equilibrium. Marine chemistry, 70(1-3), 105-119, 2000.
Lunt D. J., Foster G. L., Haywood A. M. and Stone E. J.: Late Pliocene Greenland glaciation controlled by a decline in atmospheric CO2levels. Nature 454, 1102–1105, 2008.
Lunt, D. J., Haywood, A. M., Schmidt, G. A., Salzmann, U., Valdes, P. J., & Dowsett, H. J.: Earth system sensitivity inferred from Pliocene modelling and data. Nature Geoscience, 3(1), 60-64, 2010.

Lüthi D., Le Floch M., Bereiter B., Blunier T., Barnola J. M., Siegenthaler U., Raynaud D., Jouzel J., Fischer H., Kawamura K. and Stocker T. F.: High-resolution carbon dioxide concentration record 650,000-800,000 years before present. Nature 453, 379–382, 2008.

Martínez-Botí, M. A., Marino G., Foster G. L., Ziveri P., Henehan M. J., Rae J. W. B., Mortyn P. G. and Vance D.: Boron isotope evidence for oceanic carbon dioxide leakage during the last deglaciation. Nature 518, 219–222, 2015b.

Martínez-Garcia, A., Rosell-Melé, A., Jaccard, S. L., Geibert, W., Sigman, D. M., & Haug, G. H.: Southern Ocean dust–climate coupling over the past four million years. *Nature*, *476*(7360), 312-315, 2011.

Mavromatis, V., Montouillout, V., Noireaux, J., Gaillardet, J. and Schott, J., Characterization of boron incorporation and speciation in calcite and aragonite from co-precipitation experiments under controlled pH, temperature and precipitation rate, Geochim. Cosmochim. Acta, 150, 299–313, 2015.

McCulloch M. T., Holcomb M., Rankenburg K. and Trotter J. A.: Rapid, high-precision measurements of boron isotopic compositions in marine carbonates. Rapid Commun. Mass Spectrom. 28, 2704–2712, 2014.

Medina-Elizalde M. and Lea D. W.: The mid-pleistocene transition in the tropical pacific. Science 310, 1009–1012, 2005.

Misra, S. and Froelich, P. N.: Lithium isotope history of cenozoic seawater: Changes in silicate weathering and reverse weathering. Science (80-. ). 335, 818–823, 2012.

Misra, S., Greaves, M., Owen, R., Kerr, J., Elmore, A. C. and Elderfield, H.: Determination of B/Ca of natural carbonates by HR-ICP-MS. Geochemistry, Geophys. Geosystems 15, 1617–1628, 2014a.

Misra, S., Owen, R., Kerr, J., Greaves, M. and Elderfield, H.: Determination of δ11B by HR-ICP-MS from mass limited samples: Application to natural carbonates and water samples. Geochim. Cosmochim. Acta 140, 531–552, 2014b.

Nathan, S. A., & Leckie, R. M.: Palaeogeography, Palaeoclimatology, Palaeoecology, 274(3-4), 140-159, 2009.

Ni Y., Foster G. L., Bailey T., Elliott T., Schmidt D. N., Pearson P., Haley B. and Coath C.: A core top assessment of proxies for the ocean carbonate system in surface-dwelling foraminifers. Paleoceanography 22, 2007.

Nir O., Vengosh A., Harkness J. S., Dwyer G. S. and Lahav O.: Direct measurement of the boron isotope fractionation factor: Reducing the uncertainty in reconstructing ocean paleo-pH. Earth Planet. Sci. Lett. 414, 1–5, 2015.

Nürnberg, D., Bijma, J., & Hemleben, C.: Assessing the reliability of magnesium in foraminiferal calcite as a proxy for water mass temperatures. Geochimica et Cosmochimica Acta, 60(5), 803-814, 1996.

O'Brien C. L., Foster G. L., Martínez-Botí M. A., Abell R., Rae J. W. B. and Pancost R. D.: High sea surface temperatures in tropical warm pools during the Pliocene. Nat. Geosci. 7, 606–611, 2014.

Osborne, E. B., Umling, N. E., Bizimis, M., Buckley, W., Sadekov, A., Tappa, E., Marshall, B., R. Sautter, L., Thunell, R. C.: A Sediment Trap Evaluation of B/Ca as a Carbonate System Proxy in Asymbiotic and Nondinoflagellate Hosting Planktonic Foraminifera. Paleoceanography and Paleoclimatology, 35(2), 2020.

Pagani P., Freeman G., Arthur F., Schuster M., Tiercelin J.-J. and Brunet M.: Late miocene atmospheric CO(2) concentrations and the expansion of C(4) grasses. Science 285, 876–9, 1999.

Pagani M., Liu Z., Lariviere J. and Ravelo A. C.: High Earth-system climate sensitivity determined from Pliocene carbon dioxide concentrations. Nat. Geosci. 3, 27–30, 2010.

Pagani M., Zachos J. C., Freeman K. H., Tipple B. and Bohaty S.: Atmospheric science: Marked decline in atmospheric carbon dioxide concentrations during the Paleogene. Science 309, 600–603, 2005.
Pearson, P. N., & Palmer, M. R.: Atmospheric carbon dioxide concentrations over the past 60 million years. *Nature*, *406*(6797), 695-699, 2000.
Perez, F. F., & Fraga, F.: Association constant of fluoride and hydrogen ions in seawater. Marine Chemistry, 21(2), 161-168, 1987.
Petit J. R., Jouzel J., Raynaud D., Barkov N. I., Barnola J. M., Basile I., Bender M., Chappellaz J., Davis M., Delaygue G., Delmotte M., Kotiyakov V. M., Legrand M., Lipenkov V. Y., Lorius C., Pépin L., Ritz C., Saltzman E. and Stievenard M.: Climate and atmospheric history of the past 420,000 years from the Vostok ice core, Antarctica. Nature 399, 429–436, 1999.
Pierrot, D., Lewis, E., & Wallace, D. W. R.: MS Excel program developed for CO2 system calculations. ORNL/CDIAC-105a. Carbon Dioxide Information Analysis Center, Oak Ridge National Laboratory, US Department of Energy, Oak Ridge, Tennessee, 10, 2006.
Premoli Silva, L, Haggerty, J., Rack, F., et al.: Proceedings of the Ocean Drilling Program, Initial Reports, Vol. 144, 1993.
Rae, J. W., Zhang, Y. G., Liu, X., Foster, G. L., Stoll, H. M., & Whiteford, R. D.: Atmospheric $CO_2$ over the Past 66 Million Years from Marine Archives. Annual Review of Earth and Planetary Sciences, 49, 2021.
Raitzsch M. and Hönisch B.: Cenozoic boron isotope variations in benthic foraminifers. Geology 41, 591–594, 2013.
Raitzsch M., Bijma J., Benthien A., Richter K. U., Steinhoefel G. and Kučera M.: Boron isotope-based seasonal paleo-pH reconstruction for the Southeast Atlantic – A multispecies approach using habitat preference of planktonic foraminifera. Earth Planet. Sci. Lett. 487, 138–150, 2018.
Ravelo, A. C., Lawrence, K. T., Fedorov, A., & Ford, H. L.: Comment on "A 12-million-year temperature history of the tropical Pacific Ocean". Science, 346(6216), 1467-1467, 2014.
Retallack G. J.: Greenhouse crises of the past 300 million years. Geol. Soc. Am. Bull. 121, 1441–1455, 2009.
Rickaby, R. E. M. and Halloran, P.: Cool La Nina During the Warmth of the Pliocene?, Science, 307, 1948–1952, 2005.
Ridgwell A. and Zeebe R. E.: The role of the global carbonate cycle in the regulation and evolution of the Earth system. Earth Planet. Sci. Lett. 234, 299–315, 2005.
Royer D. L.: Stomatal density and stomatal index as indicators of paleoatmospheric CO2 concentration. Rev. Palaeobot. Palynol. 114, 1–28, 2001.
Russell, A. D., Hönisch, B., Spero, H. J., & Lea, D. W.: Effects of seawater carbonate ion concentration and temperature on shell U, Mg, and Sr in cultured planktonic foraminifera. Geochimica et Cosmochimica Acta, 68(21), 4347-4361, 2004.
Schmittner, A., Urban, N. M., Shakun, J. D., Mahowald, N. M., Clark, P. U., Bartlein, P. J., Mix A. C., Rosell-Melé, A.: Climate sensitivity estimated from temperature reconstructions of the Last Glacial Maximum. *Science*, *334*(6061), 1385-1388, 2011.
Seki O., Foster G. L., Schmidt D. N., Mackensen A., Kawamura K. and Pancost R. D.: Alkenone and boron-based Pliocene pCO2records. Earth Planet. Sci. Lett. 292, 201–211, 2010.
Shackleton N.J. , Berger A., Peltier W.R,: Trans. R. Soc. Edinb. Earth Sci. 81, 251. Shipboard Leg, O. D. P., Map, O. D. P., & Map, D. S. D.: P. Initial Reports: Volume 130. doi:10.2973/odp.proc.ir.130.108.1991, 1991.

Shevenell, A. E., Kennett, J. P., & Lea, D. W.: Middle Miocene southern ocean cooling and Antarctic cryosphere expansion. *Science*, *305*(5691), 1766-1770, 2004.
Schlitzer, R., Ocean Data View, https://odv.awi.de, 2016.
Siegenthaler, U., Stocker, T. F., Monnin, E., Lüthi, D., Schwander, J., Stauffer, B, Raynaud, D., Barnola, JM., Fischer, H., Masson-Delmotte, V., Jouzel, J.: Stable carbon cycle–climate relationship during the late Pleistocene. Science, 310(5752), 1313-1317, 2005.
Sosdian, S. M., Babila, T. L., Greenop, R., Foster, G. L., & Lear, C. H.: Ocean carbon storage across the middle Miocene: A new interpretation for the Monterey Event. Nature communications, 11(1), 1-11, 2020.
Sosdian, S. M., Greenop R., Hain M. P., Foster G. L., Pearson P. N. and Lear C. H.: Constraining the evolution of Neogene ocean carbonate chemistry using the boron isotope pH proxy. Earth Planet. Sci. Lett. 498, 362–376, 2018.
Stap L. B., de Boer B., Ziegler M., Bintanja R., Lourens L. J. and van de Wal R. S. W.: $CO_2$ over the past 5 million years: Continuous simulation and new δ11B-based proxy data. Earth Planet. Sci. Lett. 439, 1–10, 2016.
Stoll, H. M., Guitian, J., Hernandez-Almeida, I., Mejia, L. M., Phelps, S., Polissar, P., Rosenthal, Y., Zhang, H. & Ziveri, P.: Upregulation of phytoplankton carbon concentrating mechanisms during low CO2 glacial periods and implications for the phytoplankton pCO2 proxy. Quaternary Science Reviews, 208, 1-20, 2019.
Super, J. R., Thomas, E., Pagani, M., Huber, M., O'Brien, C., & Hull, P. M.: North Atlantic temperature and $pCO_2$ coupling in the early-middle Miocene. *Geology*, *46*(6), 519-522, 2018.
Super, J. R., Thomas, E., Pagani, M., Huber, M., O'Brien, C. L., & Hull, P. M.: Miocene Evolution of North Atlantic Sea Surface Temperature. Paleoceanography and Paleoclimatology, 35(5), 2020.
Sutton J. N., Liu Y.-W., Ries J. B., Guillermic M., Ponzevera E. and Eagle R. A.: δ11B as monitor of calcification site pH in divergent marine calcifying organisms. Biogeosciences 15, 1447–1467, 2018.
Takahashi T., Sutherland S. C., Chipman D. W., Goddard J. G. and Ho C.: Climatological distributions of pH, pCO2, total CO2, alkalinity, and CaCO3saturation in the global surface ocean, and temporal changes at selected locations. Mar. Chem. 164, 95–125, 2014.
Tan, N., Ramstein, G., Dumas, C., Contoux, C., Ladant, J. B., Sepulchre, P., Zhang, Z., De Schepper, S.: Exploring the MIS M2 glaciation occurring during a warm and high atmospheric CO2 Pliocene background climate. Earth and Planetary Science Letters, 472, 266-276, 2017.
Tanner, T., Hernández-Almeida, I., Drury, A. J., Guitián, J., & Stoll, H.: Decreasing atmospheric $CO_2$ during the late Miocene Cooling. *Paleoceanography and Paleoclimatology*, e2020PA003925, 2020.
Tierney, J. E., Zhu, J., King, J., Malevich, S. B., Hakim, G. J., & Poulsen, C. J.: Glacial cooling and climate sensitivity revisited. *Nature*, *584*(7822), 569-573, 2020.
Thomas, E.: Descent into the Icehouse. Geology 36, 191–192, 2008.
Toggweiler, J. R.: Variation of atmospheric $CO_2$ by ventilation of the ocean's deepest water. Paleoceanography, 14(5), 571-588, 1999.
Tripati, A., & Darby, D.: Evidence for ephemeral middle Eocene to early Oligocene Greenland glacial ice and pan-Arctic sea ice. Nature communications, 9(1), 1-11, 2018
Tripati A. K., Roberts C. D. and Eagle R. A.: Coupling of CO2and Ice sheet stability over major climate transitions of the last 20 million years. Science (80 ). 326, 1394–1397, 2009.

Tripati A. K., Roberts C. D., Eagle R. A. and Li G.: A 20 million year record of planktic foraminiferal B/Ca ratios: Systematics and uncertainties in pCO2reconstructions. Geochim. Cosmochim. Acta 75, 2582–2610. http://dx.doi.org/10.1016/j.gca.2011.01.018, 2011.

Tyrrell, T., & Zeebe, R. E.: History of carbonate ion concentration over the last 100 million years. Geochimica et Cosmochimica Acta, 68(17), 3521-3530, 2004.

Van Der Burgh J., Visscher H., Dilcher D. L. and Kürschner W. M.: Paleoatmospheric signatures in Neogene fossil leaves. Science 260, 1788–1790, 1993.

Vogl J. and Rosner M.: Production and Certification of a Unique Set of Isotope and Delta Reference Materials for Boron Isotope Determination in Geochemical, Environmental and Industrial Materials. Geostand. Geoanalytical Res. 36, 161–175, 2012.

Wara M. W., Ravelo A. C. and Delaney M. L.: Climate change: Permanent El Niño-like conditions during the Pliocene warm period. Science 309, 758–761, 2005.

Yan, Y., Bender, M. L., Brook, E. J., Clifford, H. M., Kemeny, P. C., Kurbatov, A. V., Mackay, S., Mayewski, P.A., Ng, J., Severinghaus, J.P., Higgins, J. A.: Two-million-year-old snapshots of atmospheric gases from Antarctic ice. Nature, 574(7780), 663-666, 2019.

Yu, J., Elderfield, H., Greaves, M., & Day, J.: Preferential dissolution of benthic foraminiferal calcite during laboratory reductive cleaning. Geochemistry, Geophysics, Geosystems, 8(6), 2007a.

Yu J., Elderfield H. and Hönisch B.: B/Ca in planktonic foraminifera as a proxy for surface seawater pH. Paleoceanography 22, 2007.

Zachos J. C., Dickens G. R. and Zeebe R. E.: An early Cenozoic perspective on greenhouse warming and carbon-cycle dynamics. Nature 451, 279–283, 2008.

Zachos, J., Pagani, M., Sloan, L., Thomas, E., & Billups, K.: Trends, rhythms, and aberrations in global climate 65 Ma to present. science, 292(5517), 686-693, 2001.

Zeebe R. E. and Wolf-Gladrow D.: CO2 in Seawater: Equilibrium, Kinetics, Isotopes Elsevier Oceanography Series 65, Amsterdam, 2001.

Zhang Y. G., Pagani M., Liu Z., Bohaty S. M. and Deconto R.: A 40-million-year history of atmospheric CO2. Philos. Trans. R. Soc. A Math. Phys. Eng. Sci. 371, 20130096–20130096, 2013.

Zhang, Y. G., Pagani, M., & Liu, Z.: A 12-million-year temperature history of the tropical Pacific Ocean. *Science*, *344*(6179), 84-87, 2014.

Zhang, J., Wang, P., Li, Q., Cheng, X., Jin, H., & Zhang, S.: Western equatorial Pacific productivity and carbonate dissolution over the last 550 kyr: Foraminiferal and nannofossil evidence from ODP Hole 807A. Marine Micropaleontology, 64(3-4), 121-140, 2007.

## Figure captions

**Figure 1:** Modern hydrography of sites. **A.** Map of air-sea $pCO_2$ ($\Delta pCO_2$, ppm, data from Takahashi et al. (2014) and plotted using Ocean Data View from Schlitzer, (2016) showing the location of ODP Sites 806 and 807 (black circles) and Site 872 (black square, Premoli et al., 1993). Depth profiles are for preindustrial parameters, **B.** pH calculated from GLODAP database and corrected from anthropogenic inputs, **C.** Boron isotopic composition of borate ion ($\delta^{11}B_{borate}$) with associated propagated uncertainties.

**Figure 2:** Foraminiferal data for the Miocene to Recent. **A.** Benthic foraminiferal $\delta^{18}O$ data (blue line – stack from Lisiecki and Raymo, 2005; black line – compilation from Zachos et al., 2008). **B.** $\delta^{11}B$ of *T. sacculifer* (blue circles) and *G. rube*r (blue triangles) at Sites 806 (light blue), 807 (dark blue), Grey filled square are data from Site 872 located in the WEP (Sosdian et al., 2018). Open symbols are $\delta^{11}B$ data from published studies (Hönisch and Hemming, 2009; Seki et al., 2010; Foster et al., 2012; Greenop et al., 2014; Martinez-Boti et al., 2015a; Chalk et al., 2017; Dyez et al., 2018; Sosdian et al., 2018; de la Vega et al., 2020), grey open symbols are *T. sacculifer*, brown open symbols are for *G. ruber* **C.** Mg/Ca ratios of *T. sacculifer* and *G. rube*r at Sites 806, 807 and fourth-order polynomial regression from Sosdian et al. (2020) representing secular variations of $Mg/Ca_{sw}$ (blue dotted line). **E.** Calculated weight per shell for *T. sacculifer* and *G. ruber*. For Panels B-D: Circles = *T. sacculifer,* Triangles = *G. ruber.*

**Figure 3: A.** Reconstruction of surface $pCO_2$ for the past 0.8 Myr from *T. sacculifer* at ODP Sites 806 and 807. Planktonic foraminiferal $\delta^{18}O$ at site 806 with isotope stages labeled (black line – Medina-Elizalde and Lea, 2005) and benthic foraminiferal $\delta^{18}O$ stack (grey line - Lisiecki and Raymo, 2005). **B.** $pCO_2$ values calculated from boron isotopes (colored symbols - this study) with data from the literature (open gray triangles – data recalculated in Rae et al., 2021) and ice core $pCO_2$ (black line – Bereiter et al., 2015). Data from the two sites we examined reproduces the absolute values and amplitude of atmospheric $pCO_2$ as determined from ice cores, thereby validating our methodology. **C.** Cross plot for the last 0.8 Myr of $\delta^{11}B_{T.\ sacculifer}$ from this study and $\delta^{18}O_{G.\ ruber}$ from site 806 (Medina-Elizalde and Lea, 2005) (Linear regression: p=0.7). **D.** Cross plot for the last 0.8 Myr of $pCO_{2\ T.\ sacculifer}$ from this study and $\delta^{18}O_{G.\ ruber}$ from site 806 (Medina-Elizalde and Lea, 2005) (Linear regression: p=0.9) and **E.** Cross plot for the last 0.8 Myr of $pCO_{2T.\ sacculifer}$ from this study and $pCO_2$_Vostok (from ice core, Bereiter et al., 2015) (Linear regression: p=0.3, $R^2$=0.09).

**Figure 4:** Compilation of temperature from site 806 in the WEP. Mg/Ca based temperature were derived using the same framework (see supplemental information). Blue filled symbols are from Sites 806 and 807, filled gray squares are data from Site 872 (Sosdian et al., 2018). Open symbols are SST derived from Mg/Ca at Site 806 (Wara et al., 2005; Tripati et al., 2009; Nathan and Leckie, 2009). $Tex_{86}$ and $U^{K'}_{37}$ are also plotted for comparison (Zhang et al., 2014). Blue line is a smooth line (Lowess) going through the data.

**Figure 5:** Different models for the evolution of the boron geochemistry explored as part of this work. Due to the 1‰ uncertainty propagated for $\delta^{11}B_{seawater}$, all scenarios yield reconstructed seawater pH values that are within error of each other. Propagated uncertainties were calculated using eq. S14 (see Supplement). **A.** Different models for $\delta^{11}B_{seawater}$ used for the reconstruction of $pCO_2$ in this study (blue – Lemarchand et al., 2000; green – Greenop et al., 2017; red – Raitzsch and Hönisch, 2013). **B**. Reconstructed pH based on our measured $\delta^{11}B_{carbonate}$ values using different models for $\delta^{11}B_{seawater}$ (blue – Lemarchand et al., 2000; green – Greenop et al., 2017; red – Raitzsch and Hönisch, 2013), compilation pH from Sosdian et al. (2018) (open squares) and Rae et al. (2021) (open triangles) are also shown for comparison.

**Figure 6:** Different models for the evolution of a second carbonate (e.g. alkalinity) system parameter explored as part of this work. The propagated uncertainties were calculated using eq. S16 (see Supplement). **A**. Different models for alkalinity used for the reconstruction of $pCO_2$ in this study

(brown – constant alkalinity of 2330 µmol/kg, blue - Ridgwell and Zeebe, 2005; green - Tyrell and Zeebe, 2004; violet - Caves et al., 2016. Colored symbols are reconstructed $pCO_2$ based on our measured $\delta^{11}B_{carbonate}$ values , alkalinity scenario and $\delta^{11}B_{seawater}$ from Greenop et al., 2017; open squares are $pCO_2$ compilation from Sosdian et al. (2018), open triangles are from compilation from Rae et al. (2021), black symbols are from site 872. **B.** Reconstructed $pCO_2$ using constant alkalinity of 2330 µmol/kg and $\delta^{11}B_{seawater}$ from Greenop et al. (2017). **C.** Reconstructed $pCO_2$ using constant alkalinity scenario from Ridgwell and Zeebe, (2005) and $\delta^{11}B_{seawater}$ from Greenop et al. (2017). **D.** Reconstructed $pCO_2$ using constant alkalinity scenario from Tyrell and Zeebe, (2004) and $\delta^{11}B_{seawater}$ from Greenop et al. (2017). **E.** Reconstructed $pCO_2$ using constant alkalinity scenario from Caves et al., (2016) and $\delta^{11}B_{seawater}$ from Greenop et al. (2017). Stars indicate $pCO_2$ values reconstructed from alkenones by Tanner et al. (2020) (simulation 6) at Site 1088 in the Southern Ocean.

**Figure 7:** Proxy data for the past 22 million years in the Western Equatorial Pacific compared to benthic oxygen isotope data. **A.** Benthic $\delta^{18}O$ (blue line – stack from Lisiecki and Raymo, 2005; black line – compilation from Zachos et al., 2008). **B.** Benthic $\delta^{13}C$ (black line – compilation from Zachos et al., 2008). **C to E**, colored is indicating the site (filled light blue=806, filled dark blue=807), symbols represent the species (circle=*T. sacculifer* and triangle=*G. ruber*), filled grey squares are recalculated data based on Sosdian et al. (2018) at site 872. **C.** SST reconstructed at ODP Sites 806 and 807 using Mg/Ca ratios (see supplemental informations for reconstruction details), open symbols are reconstructed temperature based on litearature Mg/Ca at site 806 (see text or Fig. 4). **D.** Seawater pH reconstructed from $\delta^{11}B$ of *T. sacculifer* and *G. ruber* using $\delta^{11}B_{seawater}$ from Greenop et al. (2017) (refer to text and supplement for calculations, this study), open squares are compilation data from Sosdian et al. (2018) and open triangles are compilation from Rae et al. (2021). **E.** Reconstructed $pCO_2$ (ppm) using boron-based pH and alkalinity from Caves et al. (2016), data presented are from this study. Propagated uncertainties are given by eq. S17 for the dark blue envelope, while the light blue envelope are the uncertainties calculated based on eq. S16 (taking into account uncertainty on $\delta^{11}B_{seawater}$). Cross symbols are original $pCO_2$ calculated in Sosdian et al. (2018) at site 872; asterix symbols are calculated $pCO_2$ at site 872 from Rae et al. (2021).

**Figure 8:** Proxy data from 22 to 6 million years, including the Middle Miocene Climate Transition (MMCT) and Miocene Climate Optimum (MCO), in the Western Equatorial Pacific compared to benthic oxygen isotope data. **A.** Benthic $\delta^{18}O$ (black line – compilation from Zachos et al., 2008). **B.** Benthic $\delta^{13}C$ (black line – compilation from Zachos et al., 2008). **C and D**, colored is indicating the site (filled light blue=806, filled dark blue=807), symbols represent the species (circle=*T. sacculifer* and triangle=*G. ruber*), filled grey squares are recalculated data based on Sosdian et al. (2018) at site 872. **C**. SST reconstructed at ODP Sites 806 and 807 using Mg/Ca ratios (see supplemental informations for reconstruction details), open symbols are reconstructed temperature based on litearature Mg/Ca at site 806 (see text or Fig. 4). **D.** Reconstructed $pCO_2$ (ppm) from this study (blue symbols) using boron-based pH and alkalinity from Caves et al. (2016). Propagated uncertainties are given by eq. S17 for the dark blue envelope, while the light blue envelope reflects the uncertainties calculated based on eq. S16 (taking into account uncertainty on $\delta^{11}B_{seawater}$). Orange datapoints and envelope are calculated $pCO_2$ and associated uncertainty from our study using our framework and a constant alkalinity scenario. Open squares are compilation data from Sosdian et al. (2018). Cross symbols are original $pCO_2$ calculated in Sosdian et al. (2018) at site 872; asterix symbols are calculated $pCO_2$ at site 872 from Rae et al. (2021).

**Figure 9:** Proxy data from 7 to 1 million years, including the Warm Pliocene Transition (WPT), in the Western Equatorial Pacific compared to benthic oxygen isotope data. **A.** Benthic $\delta^{18}O$ (black line – compilation from Zachos et al., 2008). **B.** Benthic $\delta^{13}C$ (black line – compilation from Zachos et al., 2008). **C and D**, colored is indicating the site (filled light blue=806, filled dark blue=807), symbols represent the species (circle=*T. sacculifer* and triangle=*G. ruber*), filled grey squares are recalculated data based on Sosdian et al. (2018) at site 872. **C**. SST reconstructed at ODP Sites 806 and 807 using Mg/Ca ratios (see supplemental informations for reconstruction details), open symbols are reconstructed temperature based on litearature Mg/Ca at site 806 (see text or Fig. 4). **D.** Reconstructed $pCO_2$ (ppm) from this study (blue symbols) using boron-based pH and alkalinity from Caves et al.

(2016). Propagated uncertainties are given by eq. S17 for the dark blue envelope, while the light blue envelope reflects the uncertainties calculated based on eq. S16 (taking into account uncertainty on $\delta^{11}B_{seawater}$). Open squares are $pCO_2$ compilation from Sosdian et al. (2018), open triangles are from compilation from Rae et al. (2021). In black are published estimates from ice core data (circles - Yan et al., 2019).

**Figure 10:** Proxy data from 1.5 to 0.5 million years, including the Middle Pleistocene Transition (MPT), in the Western Equatorial Pacific compared to benthic oxygen isotope data. **A.** Benthic $\delta^{18}O$ (blue line – stack from Lisiecki and Raymo, 2005). **B.** Benthic $\delta^{13}C$ (black line – compilation from Zachos et al., 2008). **C and D** colored is indicating the site (filled light blue=806, filled dark blue=807), symbols represent the species (circle=*T. sacculifer* and triangle=*G. ruber*), filled grey squares are recalculated data based on Sosdian et al. (2018) at site 872. **C**. SST reconstructed at ODP Sites 806 and 807 using Mg/Ca ratios (see supplemental informations for reconstruction details), open symbols are reconstructed temperature based on litearature Mg/Ca at site 806 (see text or Fig. 4). **D.** Reconstructed $pCO_2$ (ppm) from this study (blue symbols) using boron-based pH and alkalinity from Caves et al. (2016). Propagated uncertainties are given by eq. S17. In black are published estimates from ice core data (line – Bereiter et al., 2015; black circles - Yan et al., 2019). Open triangles are from compilation from Rae et al. (2021).

**Figure 11:** Proxy data from 1.5 to 0.5 million years, including the Middle Pleistocene Transition (MPT), in the Western Equatorial Pacific compared to benthic oxygen isotope composites. **A.** Benthic $\delta^{18}O$ (blue line – compilation from Lisiecki and Raymo, 2005, black line – compilation from Zachos et al. 2008). **B.** Records from Lithium isotopes ($\delta^{7}Li$, orange, Misra and Froelich, 2012) and Strontium isotopes ($^{87/86}Sr$, grey, Hodell et al., 1991, Farrel et al., 1995, Martin et al., 1999, Martin et al., 2004), both proxies for silicate weathering. Orange arrows represent the different weathering regimes as indicated by the $\delta^{7}Li$, black crosses are indication when changes in weathering regime occurs. **C.** Reconstructed $pCO_2$ (ppm) using boron-based pH and alkalinity from Caves et al. (2016), colored is indicating the site (filled light blue=806, filled dark blue=807), symbols represent the species (circle=*T. sacculifer* and triangle=*G. ruber*), filled grey squares are recalculated data based on Sosdian et al. (2018) at site 872. Propagated uncertainties are given by eq. S17 for the dark blue envelope, while the light blue envelope are the uncertainties calculated based on eq. S16 (taking into account uncertainty on $\delta^{11}B_{seawater}$). Also shown are timing of major events. The rose band and dark rose band indicate eruption of the Columbia River flood basalts (Hooper et al., 2002) and time of maximum eruption (Kasbohm and Schoene, 2018), respectively.

**Table 1:** Core information.

| Cruise | Leg | Hole | N (°) | E (°) | Depth (m) |
|---|---|---|---|---|---|
| ODP | 130 | 807 | 3.61 | 156.62 | 2804 |
| ODP | 130 | 806 | 0.32 | 159.37 | 2520 |

**Table 2:** Comparison of reconstructed $pCO_2$ values for key intervals in the last 16 Myr.

**Mid-Pleistocene transition (1.2-0.8 Ma)**

| MIS (G) | $pCO_2$ (ppm) | Reference | MIS (IG | $pCO_2$ (ppm) | Reference | $pCO_2$ amplitude IG-G (ppm) |
|---|---|---|---|---|---|---|
| **20** | 179 | This study | **21** | 254 | This study | 75 |
| **22** | 187 | This study | **23** | 230 | This study | 43 |
| **24** | *nd* | | **25** | 298 | This study | *nd* |
| **26** | *nd* | This study | **27** | *nd* | | *nd* |
| **28** | 174 | This study | **29** | *nd* | | *nd* |
| **30** | 170 | This study | **31** | 295 | Hönisch et al., 2009 (N-TIMS) | 125 |
| **32** | 218 | Chalk et al., 2017 | **33** | 323 | Chalk et al., 2017 | 105 |
| **34** | 197 | Chalk et al., 2017 | **35** | 315 | Chalk et al., 2017 | 118 |
| **36** | 189 | Chalk et al., 2017 | **37** | 295 | This study, Chalk et al., 2017 | 106 |
| | | | **39** | 306 | This study | *nd* |

**Middle Pliocene Warm Period (3.29-2.97 Ma)**

| $pCO_2$ (ppm) | Reference |
|---|---|
| 530 ± 110 | This study (2 SD, n=4) |
| 320 ± 130 | Martinez-Boti et al., 2015b (2 SD, n=8) |
| 360 ± 85 | de la Vega et al., 2020 (2 SD, n=59) |

**Early Pliocene Warm Period (4.7-4.5 Ma)**

| $pCO_2$ (ppm) | Reference |
|---|---|
| 419 ± 119 | This study (2 SD, n=3) |

**Miocene Climate Optimum (17-14 Ma)**

| $pCO_2$ (ppm) | Reference |
|---|---|
| 511 ± 201 | This study (2 SD, n=3) |
| 350-400 | Foster et al., 2012 |
| 300-500 | Greenop et al., 2014 |
| 470-630 | Sosdian et al., 2018 |
| 687 ± 421 | Rae et al., 2021 (2 SD, n=58) |

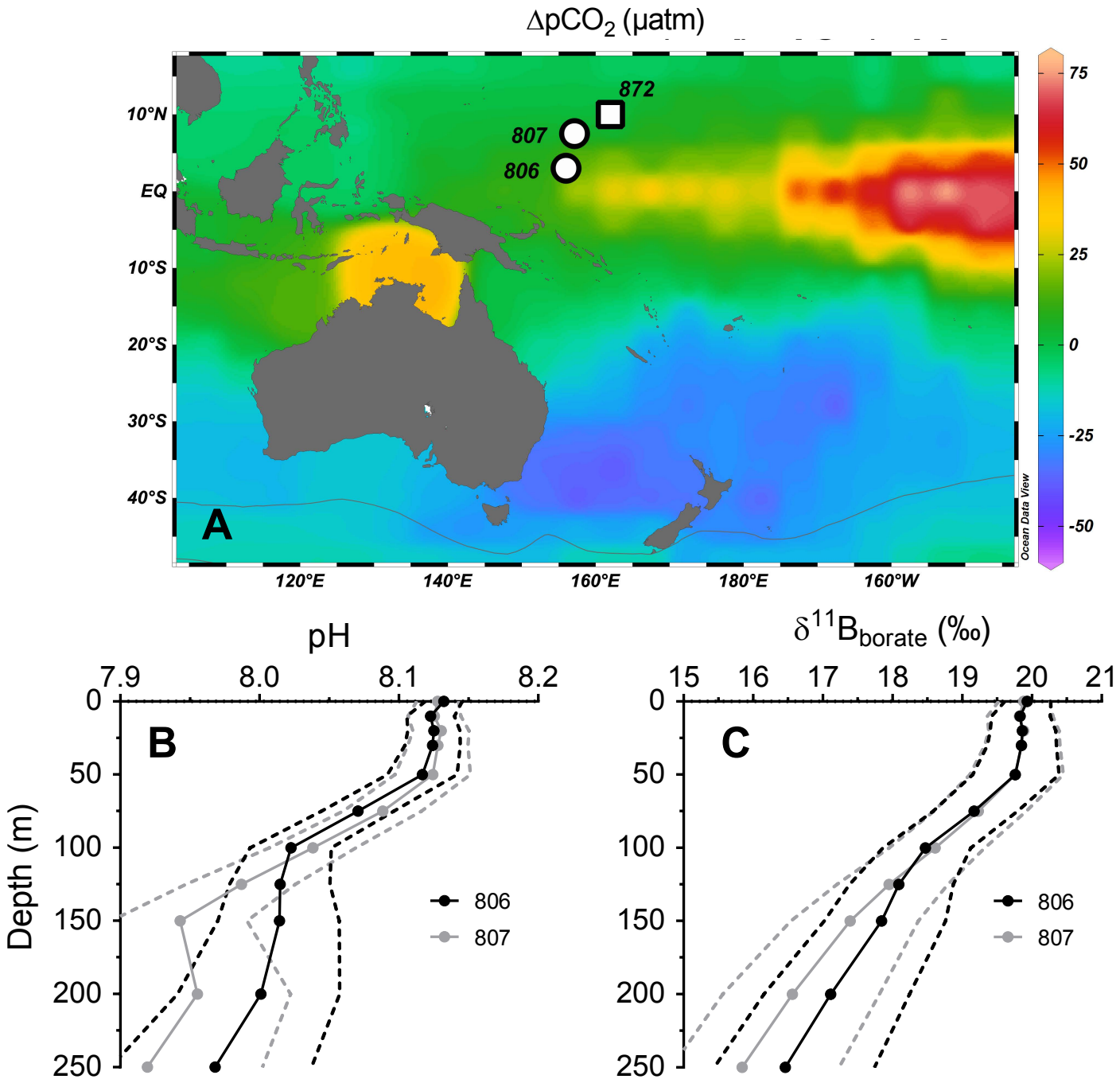
ΔpCO2 (μatm)
872
807
806
10°N
EQ
10°S
20°S
30°S
40°S
A
120°E
140°E
160°E
180°E
160°W
75
50
25
0
-25
-50
Ocean Data View
pH
7.9
8.0
8.1
8.2
B
Depth (m)
0
50
100
150
200
250
806
807
δ11Bborate (‰)
15
16
17
18
19
20
21
C
806
807

Figure 1

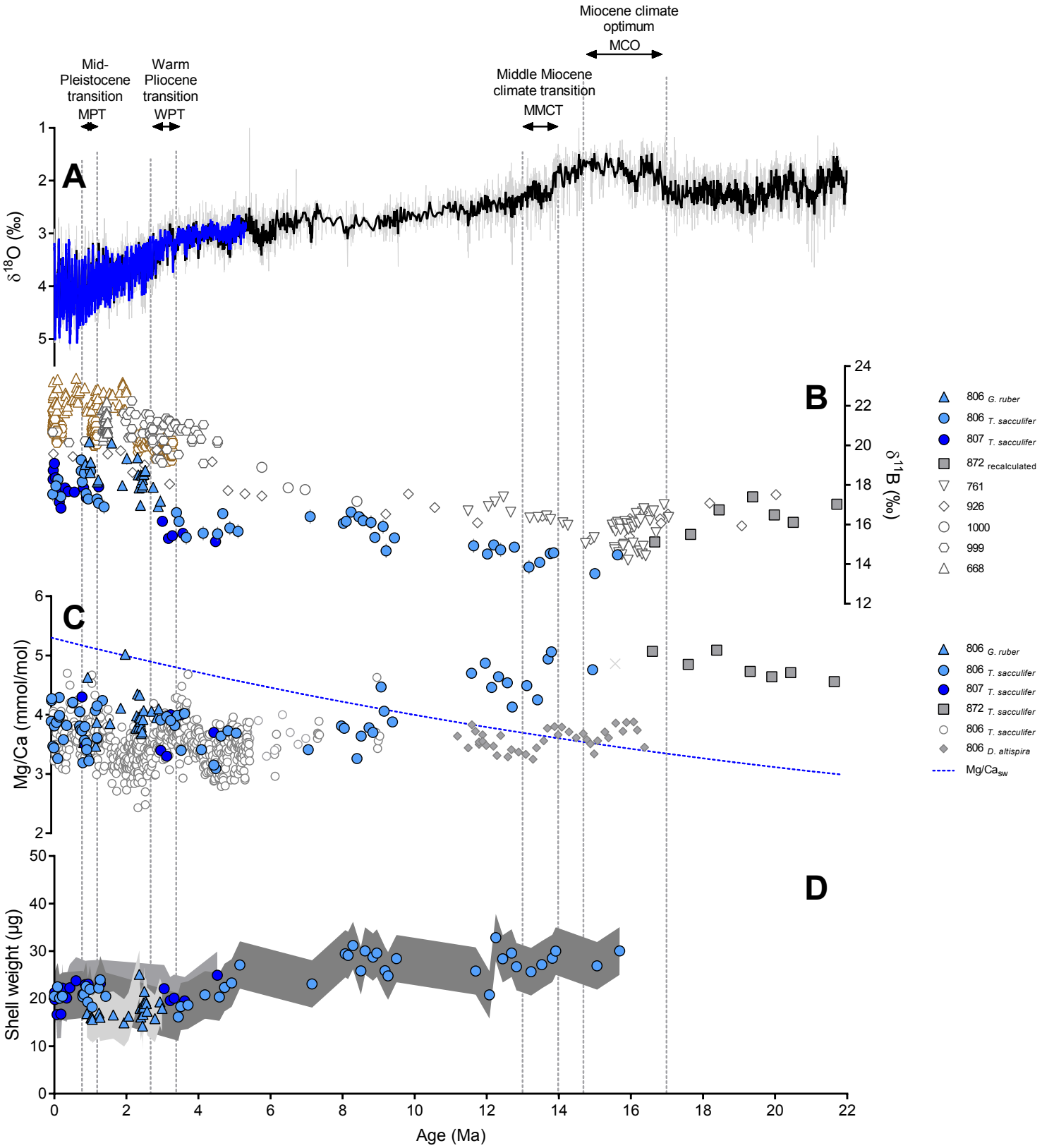
Miocene climate optimum
MCO
Mid-Pleistocene transition
MPT
Warm Pliocene transition
WPT
Middle Miocene climate transition
MMCT
A
δ18O (‰)
B
δ11B (‰)
806 G. ruber
806 T. sacculifer
807 T. sacculifer
872 recalculated
761
926
1000
999
668
C
Mg/Ca (mmol/mol)
806 G. ruber
806 T. sacculifer
807 T. sacculifer
872 T. sacculifer
806 T. sacculifer
806 D. altispira
Mg/Casw
D
Shell weight (µg)
Age (Ma)

Figure 2

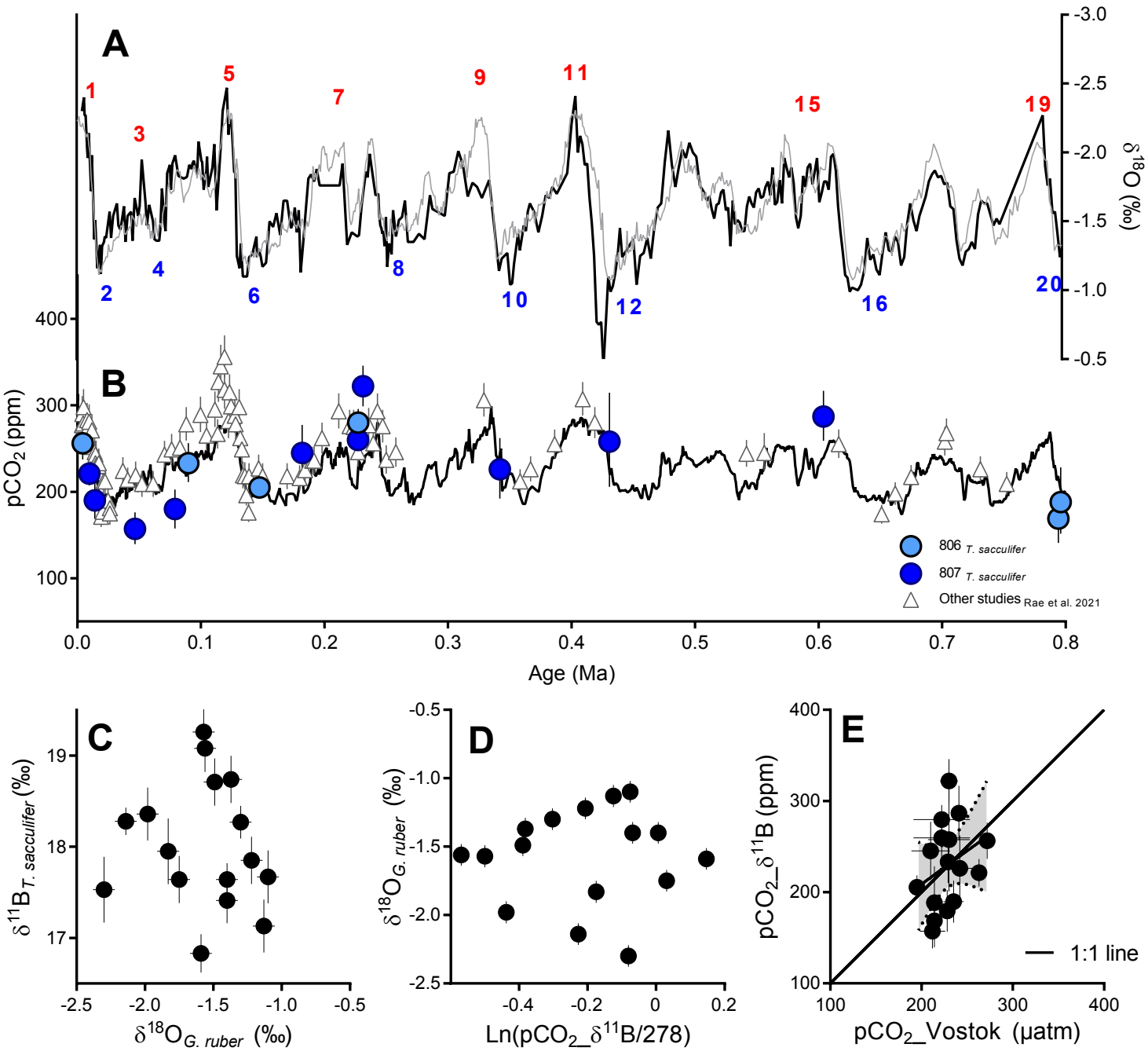
A
B
C
D
E
1
2
3
4
5
6
7
8
9
10
11
12
15
16
19
20
-3.0
-2.5
-2.0
-1.5
-1.0
-0.5
δ18O (‰)
400
300
200
100
pCO2 (ppm)
0.0
0.1
0.2
0.3
0.4
0.5
0.6
0.7
0.8
Age (Ma)
806 T. sacculifer
807 T. sacculifer
Other studies Rae et al. 2021
19
18
17
δ11BT. sacculifer (‰)
-2.5
-2.0
-1.5
-1.0
-0.5
δ18OG. ruber (‰)
-0.5
-1.0
-1.5
-2.0
-2.5
δ18OG. ruber (‰)
-0.4
-0.2
0
0.2
Ln(pCO2_δ11B/278)
400
300
200
100
pCO2_δ11B (ppm)
100
200
300
400
pCO2_Vostok (µatm)
1:1 line

Figure 3

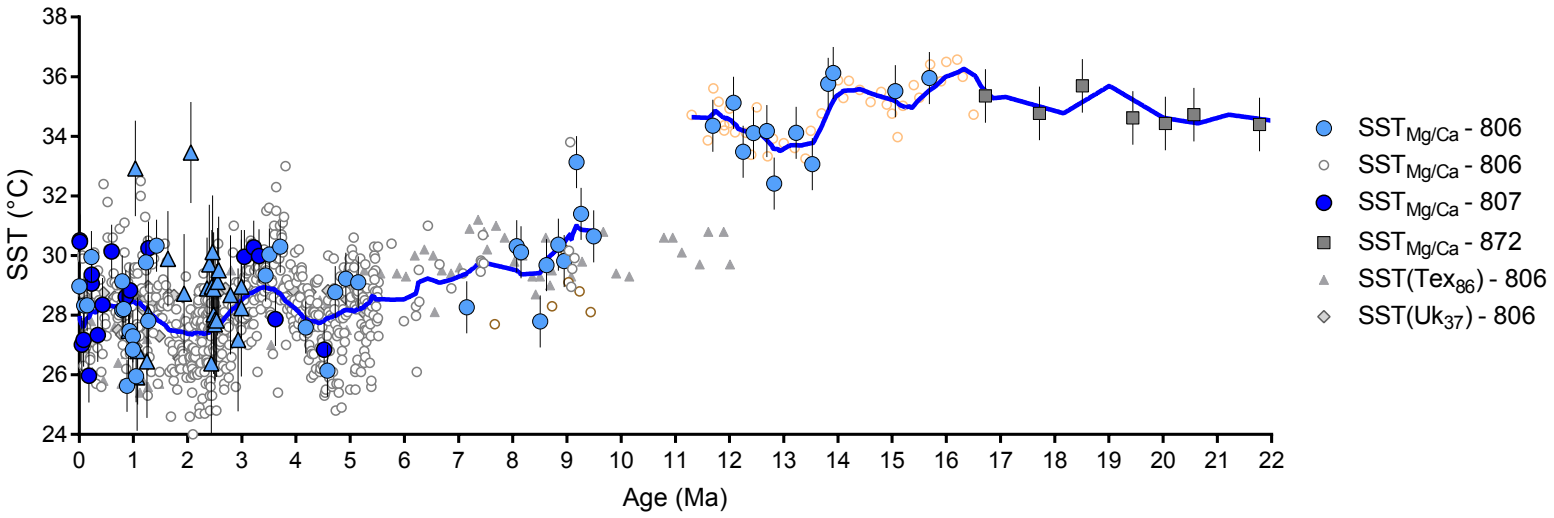
SST (°C)
Age (Ma)
SST$_{Mg/Ca}$ - 806
SST$_{Mg/Ca}$ - 806
SST$_{Mg/Ca}$ - 807
SST$_{Mg/Ca}$ - 872
SST(Tex$_{86}$) - 806
SST(Uk$_{37}$) - 806

Figure 4

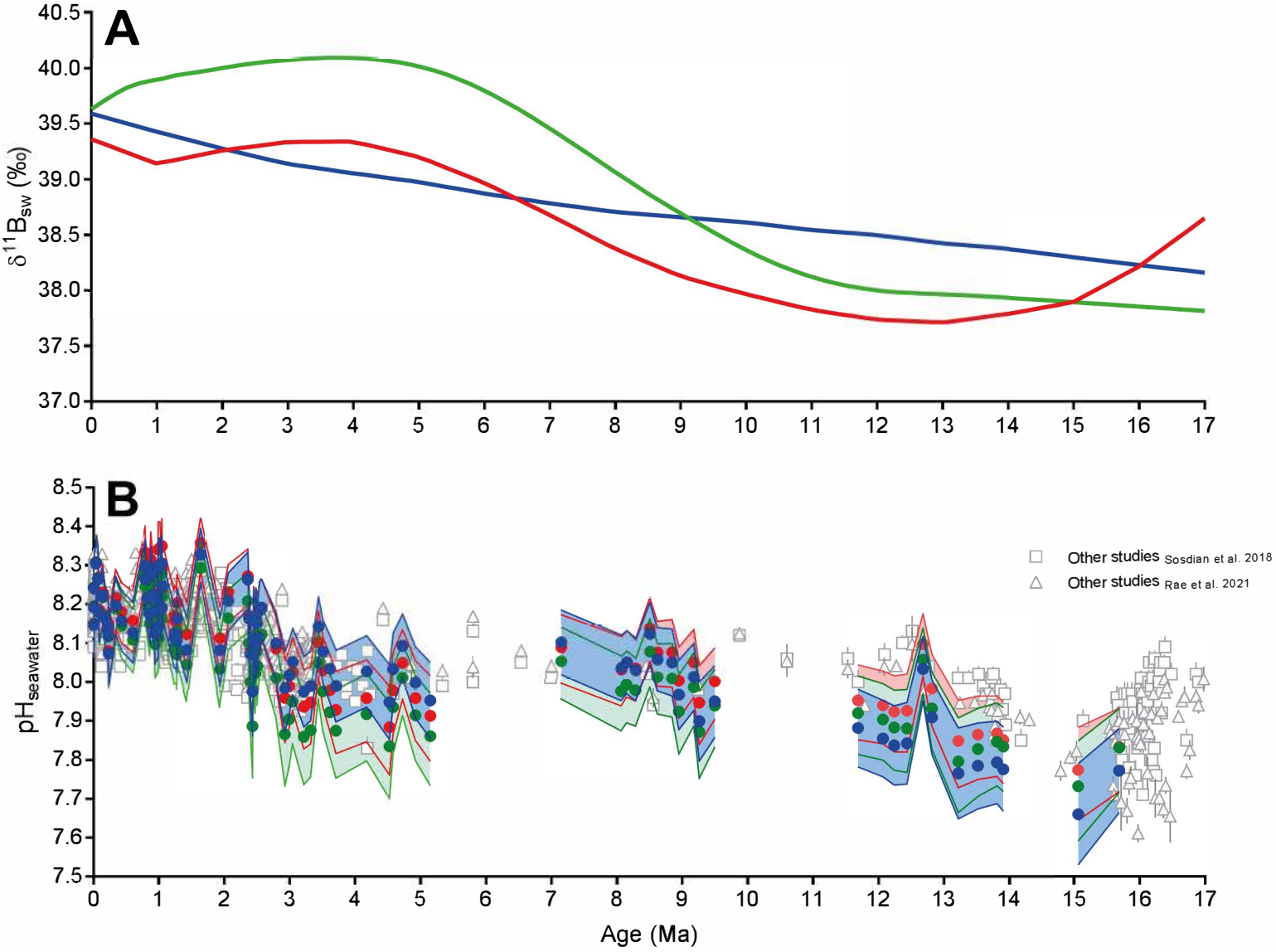
A
$\delta^{11}B_{sw}$ (‰)
40.5
40.0
39.5
39.0
38.5
38.0
37.5
37.0
0 1 2 3 4 5 6 7 8 9 10 11 12 13 14 15 16 17
B
$pH_{seawater}$
8.5
8.4
8.3
8.2
8.1
8.0
7.9
7.8
7.7
7.6
7.5
Other studies Sosdian et al. 2018
Other studies Rae et al. 2021
0 1 2 3 4 5 6 7 8 9 10 11 12 13 14 15 16 17
Age (Ma)

Figure 5

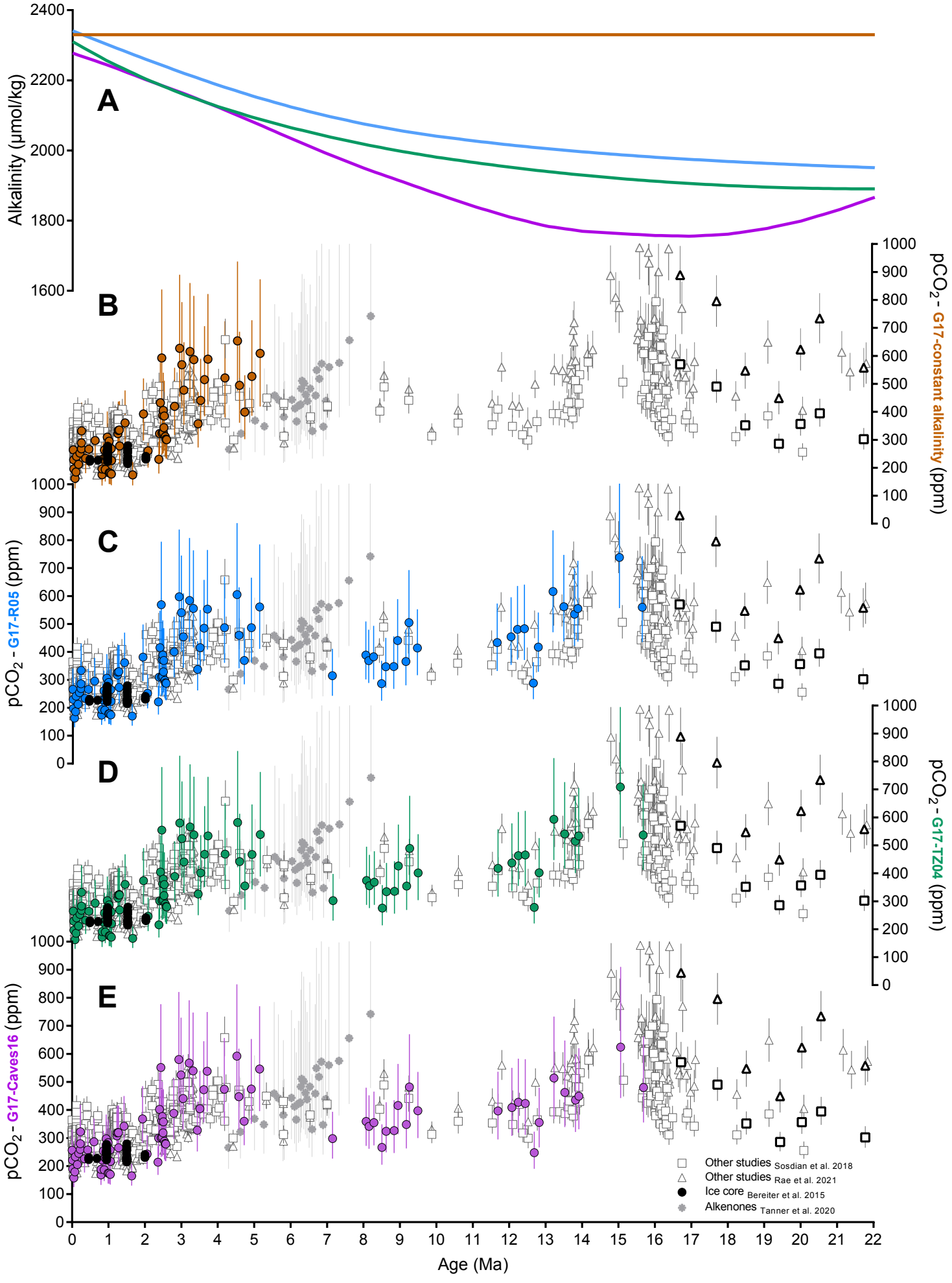
A
B
C
D
E
Alkalinity (µmol/kg)
2400
2200
2000
1800
1600
pCO2 - G17-constant alkalinity (ppm)
pCO2 - G17-R05 (ppm)
pCO2 - G17-TZ04 (ppm)
pCO2 - G17-Caves16 (ppm)
1000
900
800
700
600
500
400
300
200
100
0
Other studies Sosdian et al. 2018
Other studies Rae et al. 2021
Ice core Bereiter et al. 2015
Alkenones Tanner et al. 2020
0
1
2
3
4
5
6
7
8
9
10
11
12
13
14
15
16
17
18
19
20
21
22
Age (Ma)

Figure 6

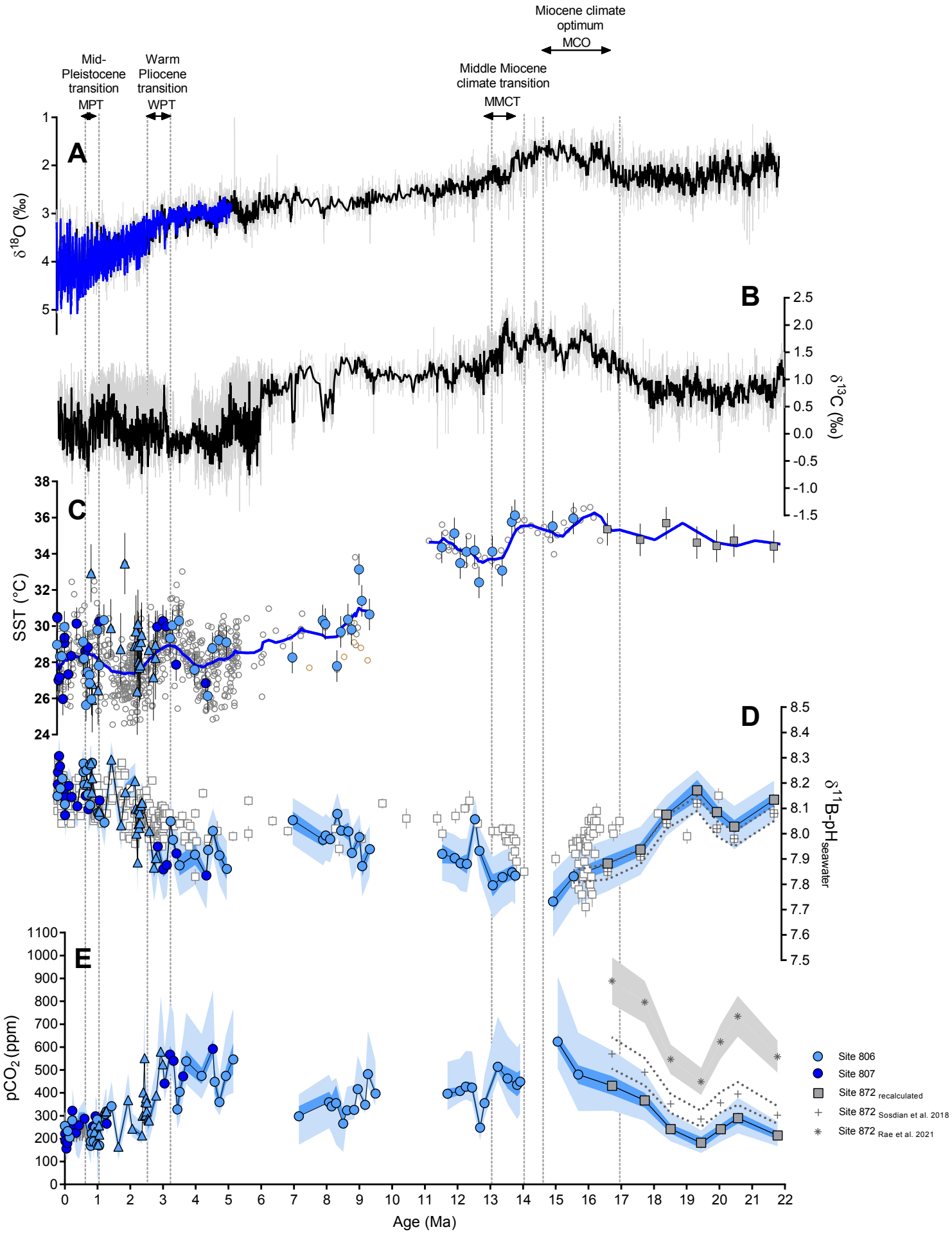
Miocene climate optimum
MCO
Mid-Pleistocene transition
MPT
Warm Pliocene transition
WPT
Middle Miocene climate transition
MMCT
A
B
C
D
E
δ18O (‰)
δ13C (‰)
SST (°C)
δ11B-pHseawater
pCO2 (ppm)
Age (Ma)
Site 806
Site 807
Site 872 recalculated
Site 872 Sosdian et al. 2018
Site 872 Rae et al. 2021

Figure 7

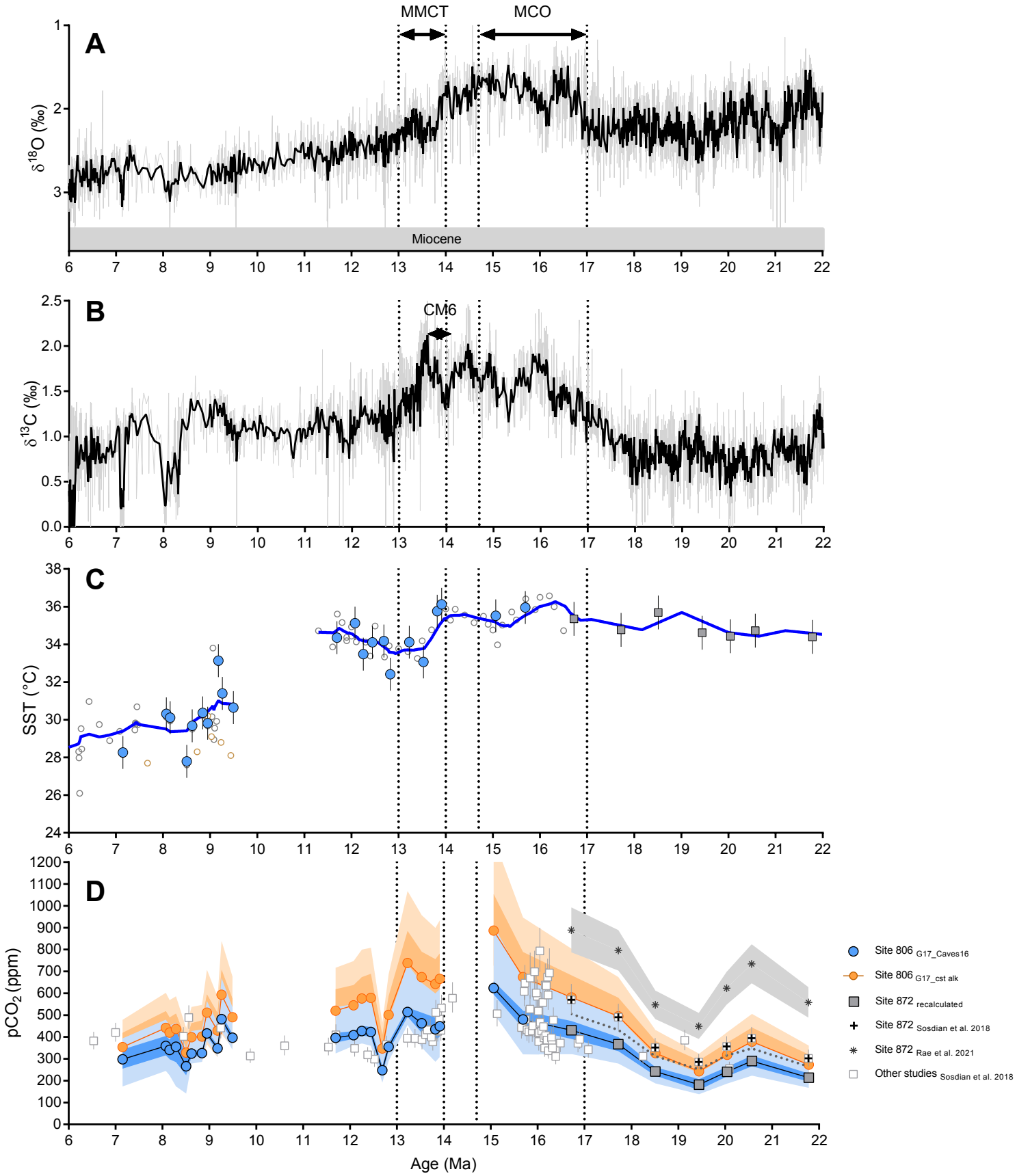
A
MMCT
MCO
Miocene
δ18O (‰)
B
CM6
δ13C (‰)
C
SST (°C)
D
pCO2 (ppm)
Age (Ma)
Site 806 G17_Caves16
Site 806 G17_cst alk
Site 872 recalculated
Site 872 Sosdian et al. 2018
Site 872 Rae et al. 2021
Other studies Sosdian et al. 2018

Figure 8

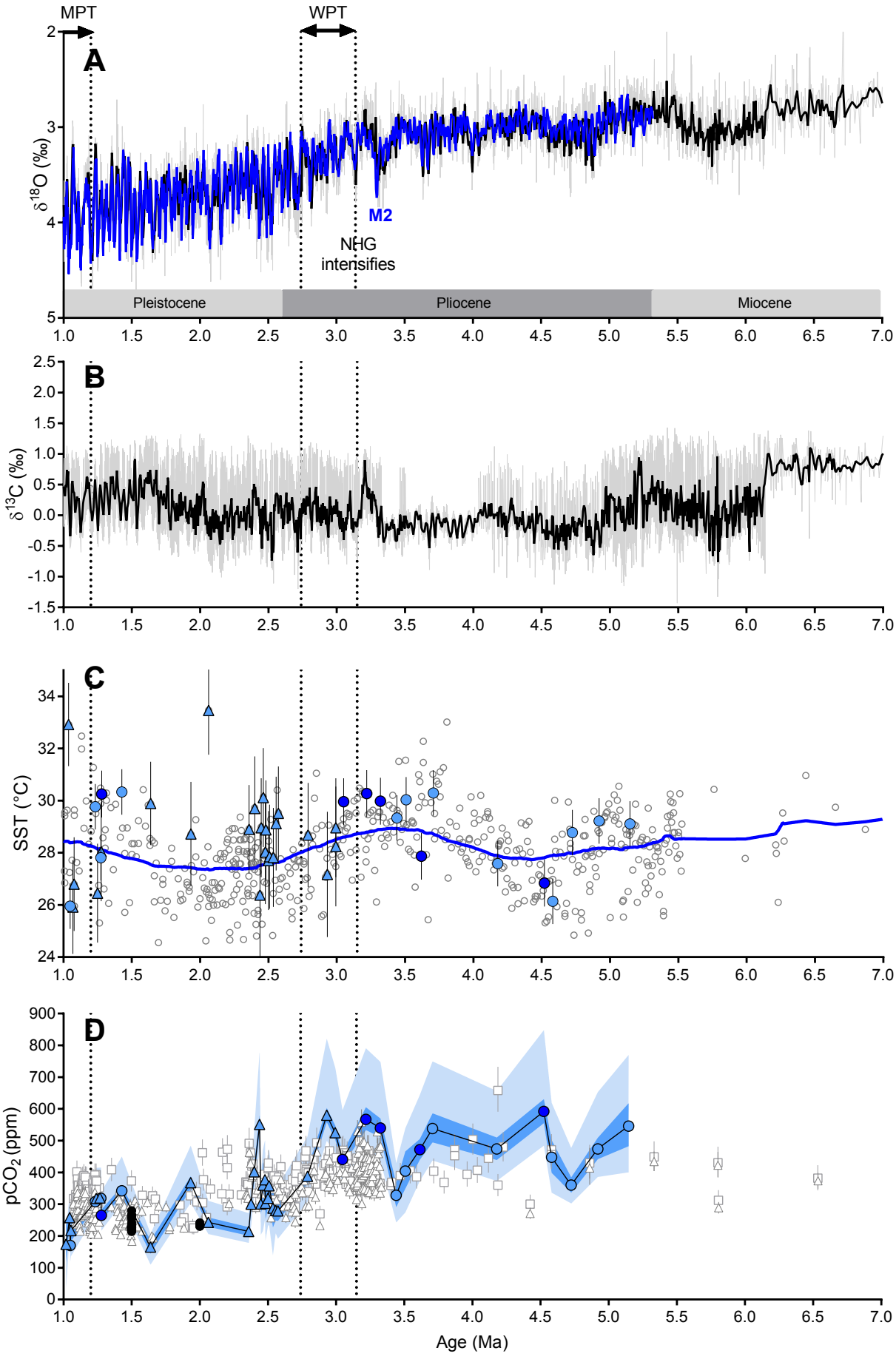
MPT
WPT
A
M2
NHG
intensifies
Pleistocene
Pliocene
Miocene
δ18O (‰)
B
δ13C (‰)
C
SST (°C)
D
pCO2 (ppm)
Age (Ma)
Site 806
Site 807
Other studies Sosdian et al. 2018
Other studies Rae et al. 2021
Ice core Bereiter et al. 2015

Figure 9

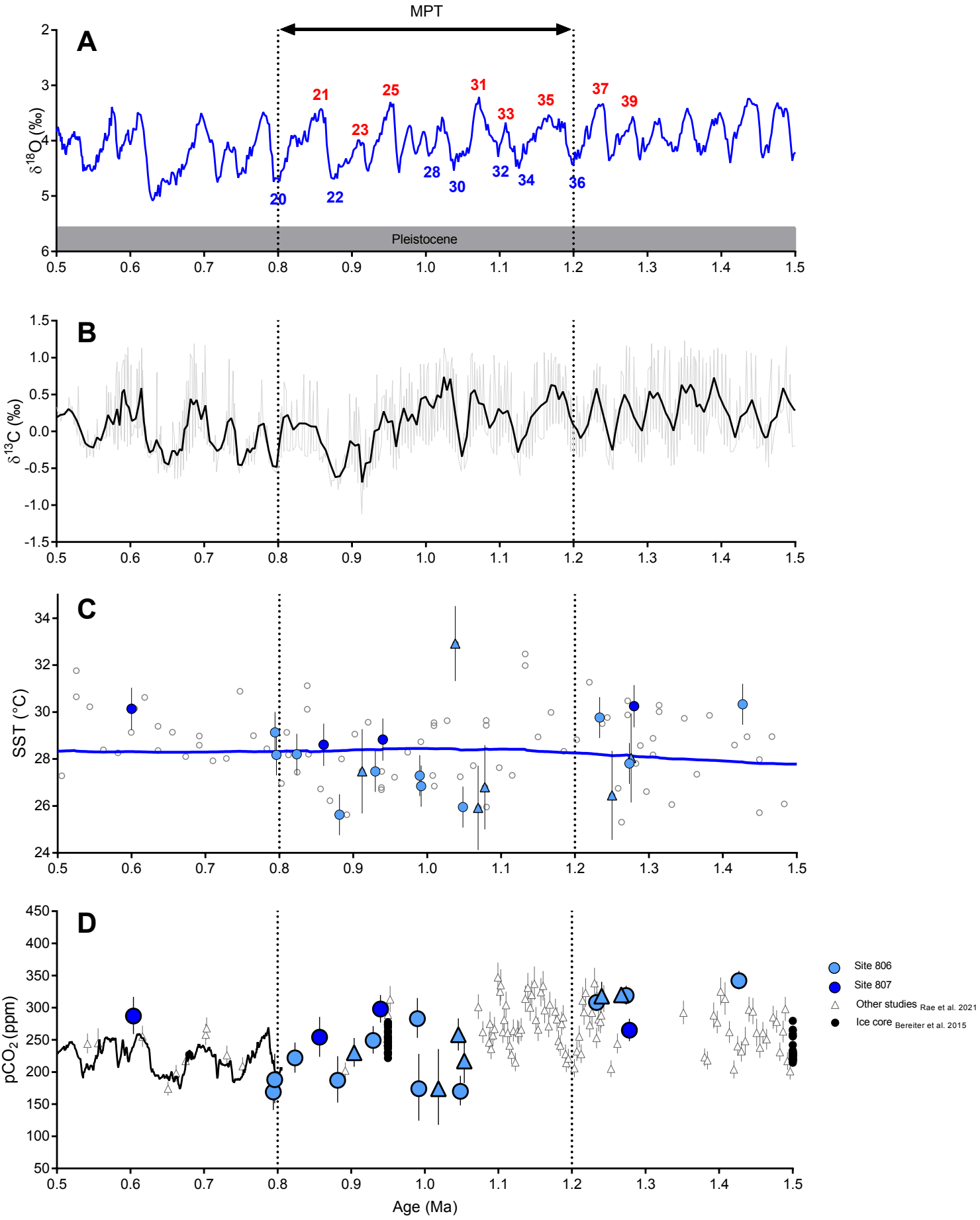
MPT
A
B
C
D
$\delta^{18}O$ (‰)
$\delta^{13}C$ (‰)
SST (°C)
$pCO_2$ (ppm)
Age (Ma)
Pleistocene
20
21
22
23
25
28
30
31
32
33
34
35
36
37
39
Site 806
Site 807
Other studies Rae et al. 2021
Ice core Bereiter et al. 2015

Figure 10

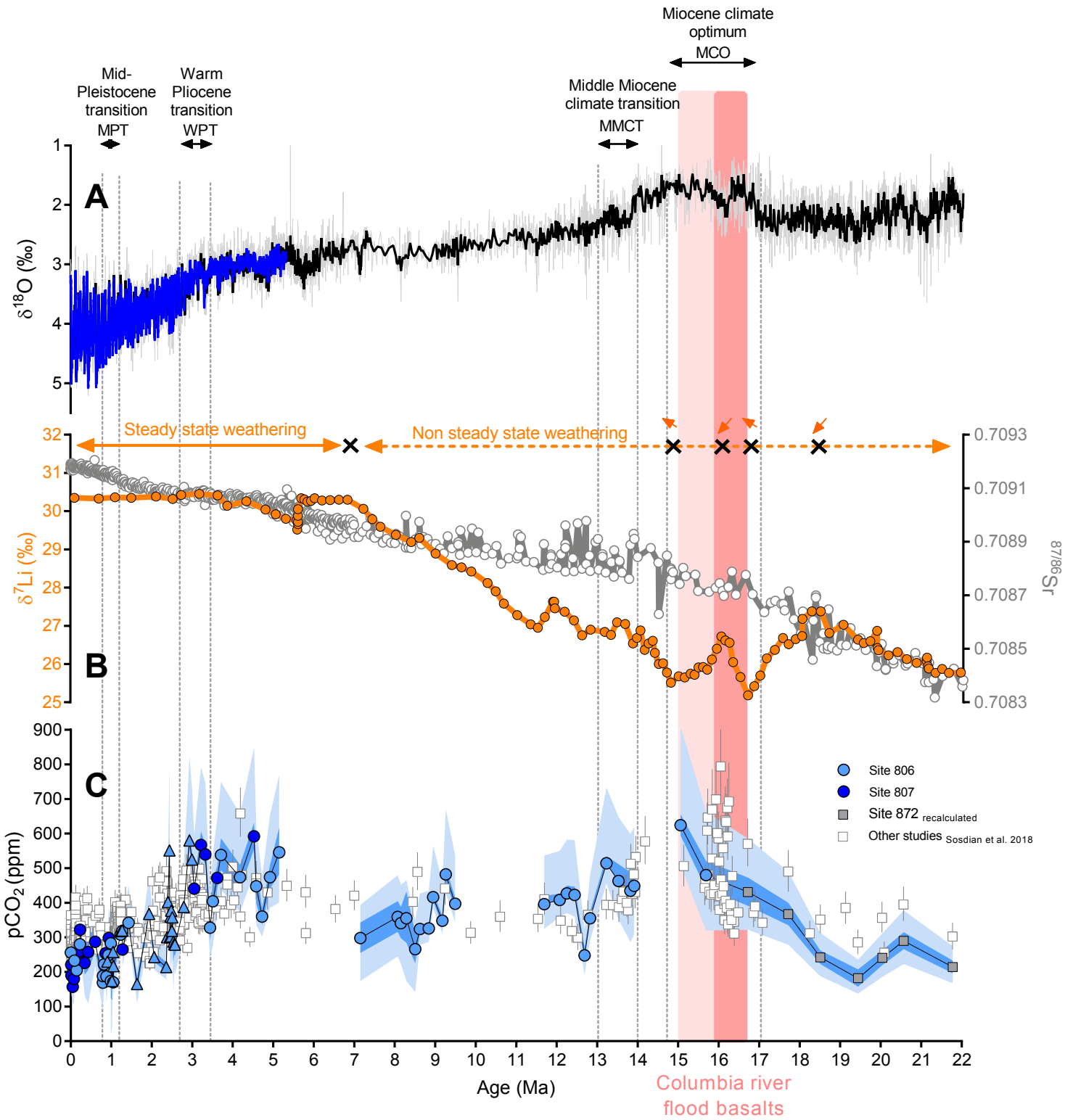
Miocene climate optimum
MCO
Mid-Pleistocene transition
MPT
Warm Pliocene transition
WPT
Middle Miocene climate transition
MMCT
A
$\delta^{18}O$ (‰)
Steady state weathering
Non steady state weathering
B
$\delta^{7}Li$ (‰)
$^{87}Sr/^{86}Sr$
C
$pCO_2$ (ppm)
Site 806
Site 807
Site 872 recalculated
Other studies Sosdian et al. 2018
Age (Ma)
Columbia river flood basalts

Figure 11